Multiphase equation of state for carbon addressing high pressures and temperatures

Lorin X. Benedict,[1] Kevin P. Driver,[2] Sebastien Hamel,[1] Burkhard Militzer,[2,3] Tingting Qi,[1] Alfredo A. Correa,[1] A. Saul,[4,5,6] and Eric Schwegler[1]

[1]*Condensed Matter and Materials Division, Physical and Life Sciences Directorate, Lawrence Livermore National Laboratory, Livermore, California 94550, USA*

[2]*Department of Earth and Planetary Science, University of California at Berkeley, Berkeley, California 94720, USA*

[3]*Department of Astronomy, University of California at Berkeley, Berkeley, California 94720, USA*

[4]*Aix-Marseille University, CINaM-CNRS UMR 7325 Campus de Luminy, 13288 Marseille cedex 9, France*

[5]*Department of Civil and Environmental Engineering, Massachusetts Institute of Technology, 77 Massachusetts Avenue, Cambridge, Massachusetts 02139, USA*

[6]*MultiScale Material Science for Energy and Environment, UMI 3466 CNRS-MIT, 77 Massachusetts Avenue, Cambridge, Massachusetts 02139, USA*

(Received 21 October 2013; revised manuscript received 17 May 2014; published 30 June 2014)

We present a 5-phase equation of state for elemental carbon which addresses a wide range of density and temperature conditions: 3g/cc $< \rho <$ 20g/cc, 0 K $< T < \infty$. The phases considered are diamond, BC8, simple cubic, simple hexagonal, and the liquid/plasma state. The solid phase free energies are constrained by density functional theory (DFT) calculations. Vibrational contributions to the free energy of each solid phase are treated within the quasiharmonic framework. The liquid free energy model is constrained by fitting to a combination of DFT molecular dynamics performed over the range 10 000 K $< T <$ 100 000 K, and path integral quantum Monte Carlo calculations for $T >$ 100 000 K (both for ρ between 3 and 12 g/cc, with select higher-ρ DFT calculations as well). The liquid free energy model includes an atom-in-jellium approach to account for the effects of ionization due to temperature and pressure in the plasma state, and an ion-thermal model which includes the approach to the ideal gas limit. The precise manner in which the ideal gas limit is reached is greatly constrained by both the highest-temperature DFT data and the path integral data, forcing us to discard an ion-thermal model we had used previously in favor of a new one. Predictions are made for the principal Hugoniot and the room-temperature isotherm, and comparisons are made to recent experimental results.

DOI: 10.1103/PhysRevB.89.224109 PACS number(s): 64.30.−t, 64.70.dm, 64.70.K−, 65.20.De

I. INTRODUCTION

The high-pressure and high-temperature equation of state (EOS) and phase diagram of carbon have received considerable attention of late. Recent laser-shock and ramp-compression studies [1–7], together with shock measurements performed with magnetically driven flyer plates [8], have produced data in the range from $P =$ 0–50 Mbar. In addition, theoretical work on the EOS and phase diagram in this same range has yielded predictions which are largely (though not completely) in accord with these experimental data [8,9]. These studies were conducted with density functional theory (DFT) molecular dynamics (MD). Much of this recent focus on the carbon EOS, specifically in states of compression reached when starting in the diamond phase, has arisen from the interest of using high-density carbon as an ablator material for capsules designed to achieve fusion at the National Ignition Facility [10]. While these experimental and theoretical studies have been useful in constraining the EOS of carbon for this and related applications, it is crucial to note that the states reached by the ablator in inertial confinement fusion (ICF) are expected to include temperatures in excess of tens of eV [10]. Such conditions have not yet been sufficiently characterized.

At such high temperatures, DFT-MD is extremely challenging to perform, due to the large number of high-lying, partially occupied single-electron states that must be included for an accurate rendering of electronic excitations. Indeed, an orbital-free variant of DFT-MD has been developed and used to handle such high-temperature applications [11], but as yet, a satisfactory treatment of atomic shell structure in this approach is lacking. The approach as implemented thus far [11] is (somewhat) reminiscent of a Thomas-Fermi treatment for the electrons [12]. Another altogether different approach to describing the electronic structure of the high-T plasma state is path integral Monte Carlo (PIMC) [13]. In this approach, unlike in typical implementations of DFT, there is no mean-field assumption made for the many-electron problem, and the imaginary time treatment makes high-T simulations more efficient to perform than low-T simulations. Although assumptions regarding the nodal surface of the many electron density matrix necessarily introduce approximations for the treatment of atomic shells, it is very encouraging that recent work on the C plasma has demonstrated that EOS predictions can be made with this method which smoothly interpolate between DFT-MD results at the lower temperatures and the high-T Debye-Hückel limit [14].

The ultrahigh-pressure regime near $T = 0$ has been studied recently as well, using *ab initio* electronic structure techniques of the DFT variety together with a random search method to find the thermodynamically stable crystalline phases at pressures between 10 and 1000 Mbar [15]. This work extended earlier quantitative studies of the C phase diagram that treated the diamond and BC8 phases up to $P \sim 20$ Mbar [16]. The random search established the sequence of stable phases to be diamond → BC8 → (slight modification of) simple cubic (sc) → simple hexagonal (sh) → face-centered cubic (fcc) [15]. Though these authors did not attempt to predict the details of

the C melt curve in these extreme conditions, their analysis using a quasiharmonic description of the phonons for these solid phases suggested the existence of a BC8-sc-sh triple point, as seen in Fig. 3 of their paper [15].

A few years ago, Correa *et al.* used the available theoretical understanding of the C phase diagram at the time [16] to produce a three-phase EOS model for C focusing specifically on the regime of $P = 0$–20 Mbar and $T = 0$–20 000 K [9]. The phases considered were diamond, BC8, and the liquid. The individual phase free energy models were fitted to the results of DFT-MD calculations. Since the final multiphase EOS model was designed to be used in continuum dynamics (hydrocode) simulations spanning a wider range of conditions, these researchers embedded their detailed three-phase EOS model into a more coarse-grained model [17] that respected the ideal gas limits at high T and low ρ and the Thomas-Fermi limit [12] at high ρ. While satisfactory in a broad sense, this older EOS model suffers from three main drawbacks: (1) The embedding of the DFT-based 3-phase model into the coarse-grained model created kinks in the thermodynamic functions, even though an attempt was made to smooth out such features by interpolation. (2) There are no solid phases beyond BC8; sc and sh phases, for instance, are not included. (3) The electronic excitations of the high-T liquid are treated with an average-atom Thomas-Fermi model, so atomic shell structure is not included in sufficient detail.

In this work, we remedy these deficiencies by constructing a 5-phase EOS for C, again based on *ab initio* calculations (for densities between $\sim$ 1 and 25 g/cc), in which the free energy models for each phase are defined over wide ranges of ρ and T and exhibit sensible limiting behavior. No embedding into a simpler model [17] is performed. The two extra phases included are the sc and sh phases. While our phase diagram differs slightly from that of Ref. [15], the inclusion of these extra phases allows our EOS to be in accord with *ab initio* predictions for pressures up to well over 100 Mbar. The EOS of the high-temperature liquid is elucidated by performing DFT-MD for C up to 100 000 K and PIMC calculations [14] from $\sim$200 000 K (depending on the density) to over 10^8 K. We establish that the best fit to these EOS predictions requires a liquid free energy model in which (1) electronic excitations are treated in an average-atom picture which includes atomic shell structure, and (2) the decay of the ion-thermal specific heat from $3k_B$/atom to $3k_B/2$/atom as $T \to \infty$ is much faster than previously expected. In what follows, we describe the details of our DFT and PIMC calculations of the EOS of C, present the models we use to fit these *ab initio* data, and compare various thermodynamic tracks through our resulting EOS with the findings of recent experiments performed on high-energy laser platforms [1,6,7].

II. THEORY AND SIMULATION

Our computational results fall into two categories: (1) calculations of the EOS, by which we mean internal energy E and pressure P as functions of density ρ and temperature T, and (2) calculations of intermediate quantities which we use to build the EOS. These include cold compression curves (E and P as functions of ρ, for ions fixed in position [18]), phonon densities of states (PDOSs), and electronic excitation

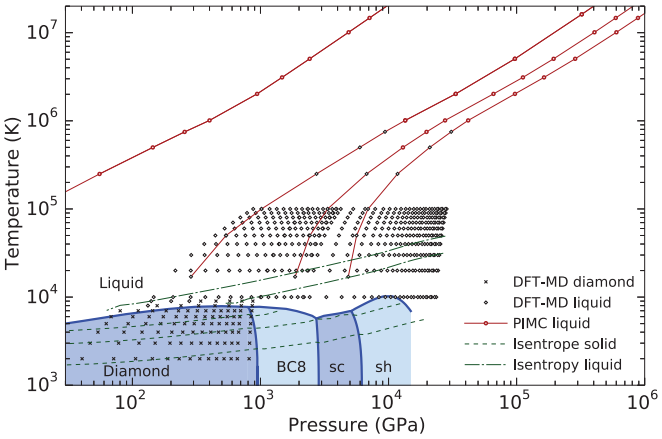

FIG. 1. (Color online) Predicted C phase diagram (see subsequent sections) along with the DFT-MD (black open symbols for liquid, black crosses for solid) and PIMC (red open symbols) data we use to validate our EOS model. Note that the four isochores with densities 0.1 g/cc, 3.18 g/cc, 8.5 g/cc, and 11.18 g/cc (red lines) contain DFT-MD points for lower T and PIMC points for higher T. Also shown are portions of five isentropes (green lines) computed from our EOS model with entropy values increasing from the bottom: 3.78 k_B/atom, 5.49 k_B/atom, 6.61 k_B/atom, 12.56 k_B/atom, and 12.72 k_B/atom. Note that the 0.1 g/cc isochore (upper leftmost red curve) exists throughout a range in which the EOS model of this work is *not* valid.

contributions to the free energy. The first category of quantities we extract from DFT-MD (for solid and liquid phases) and PIMC (liquid phase). The second group of quantities we extract solely from DFT calculations for the solid phases. Figure 1 shows the locations of our DFT-MD and PIMC simulation points in the (P,T) plane. Also shown for reference are our predicted C phase lines, presented and discussed in detail below, as well as portions of five separate isentropes computed from the EOS model described in this work. We stress that while the DFT-MD results are concentrated entirely in the diamond and liquid phases (with the exception of a few points within the stability fields of sc and sh), we use the aforementioned DFT-derived intermediate quantities (cold curves, PDOSs, etc.) to constrain the EOS model for each of the four solid phases considered here. All of our DFT-MD and PIMC data, consisting of internal energy and pressure at different densities and temperatures, are reproduced in tables contained in the Supplemental Material [19]. In the following two subsections, we describe in detail our approaches to obtaining these data.

A. DFT calculations

With DFT methods, we perform calculations of cold compression curves $[E(\rho,T=0), P(\rho,T=0)]$, phonon densities of states, electronic excitation contributions to the free energy, and the EOS itself (E and P as functions of ρ and T). We also present a limited number of calculations of ionic diffusivity, from which we can infer melt behavior. For all of these, we use the VASP code [20], together with projector augmented wave (PAW) pseudopotentials [21]. We use a "hard" PAW with a core radius of 1.1 bohrs and 4 valence electrons

and the generalized gradient approximation (GGA) of DFT with the Perdew-Burke-Ernzerhof (PBE) exchange correlation functional [22]. The plane-wave cutoff is set to 1300 eV. In addition, we test the sensitivity of our results to the choice of PAW by comparing to even harder PAWs with 0.8 bohr core radii and 6 valence electrons. We also investigate the use of a so-called van der Waals exchange-correlation functional [23] in the calculation of the cold curves.

For the phonon calculations, we use the primitive cell with a Monkhorst-Pack [24] k-point grid of $40\times40\times40$ for the simple cubic (sc) and the simple hexagonal (sh) phases and for fcc. The calculations on the sh phase are done with a c/a ratio of 0.986 evaluated by performing cell optimization for several compressions. No appreciable variation in the c/a ratio with volume was observed. For the diamond and BC8 phases we used an 8 atom unit cell with a $20\times20\times20$ k-point grid. For the sc phase, we compared our results to those with a 2 atom unit cell with a pmma space group (tetragonal distortion) [15] which was calculated with a $20\times40\times40$ k-point grid.

For the molecular dynamics simulations, we use 64 atoms and perform Born-Oppenheimer MD (BOMD) within the *NVT* ensemble with a Nosé-Hoover thermostat [25]. The Mermin formulation of DFT [26] is used, in which Kohn-Sham single-particle states are occupied by a Fermi-Dirac distribution at the chosen temperature. We use a time step of 0.75 fs in order to converge the internal energy and pressure to the desired accuracy. The electronic density is constructed from single-particle wave functions by sampling at the $(\frac{1}{4},\frac{1}{4},\frac{1}{4})$ point of the Brillouin zone. The electron occupation numbers are taken to be a Fermi-Dirac distribution set at the average temperature of the ions. For the different densities and temperatures, we use a sufficient number of bands such that we have at least 40 bands with occupation numbers smaller than 0.00001. The MD is run for 10 000 steps with the last 5000 steps used for averaging the internal energy and the pressure.

The use of pseudopotentials under extreme conditions of pressure and temperature can be problematic. For high compressions or high temperatures the interatomic distances can become smaller than the diameter of the PAW sphere. In Fig. 2, we plot the pair distribution functions for the densities 26.59 g/cc, 16.48 g/cc, and 6.93 g/cc and temperatures of 50 000 K and 100 000 K, where clearly the PAW spheres overlap significantly (the black and blue dashed vertical lines are the diameter of the 1.1 and 0.8 bohr PAW potentials, respectively; see below). At higher temperatures still, the thermal excitations of the 1s electrons can no longer be neglected. Such situations should be addressed by having all 6 electrons in the valence. However, for the current DFT-MD calculations, we find this not to be necessary for temperatures of 100 000 K or lower.

In order to assess the sensitivity of our results to the PAW potential chosen, we construct PAW potentials with different cutoff radii, which range from 1.1 to 0.8 bohr radii. The Vanderbilt projectors generation scheme is utilized [27]. As the cutoff radii decrease, in order to maintain and optimize the PAW performance, we add additional partial waves for both s and p angular momenta. Different sets of reference energies are chosen, which are determined not to affect our computational results. Moreover, when the carbon-carbon distance is sufficiently small, the 1s core state is included as

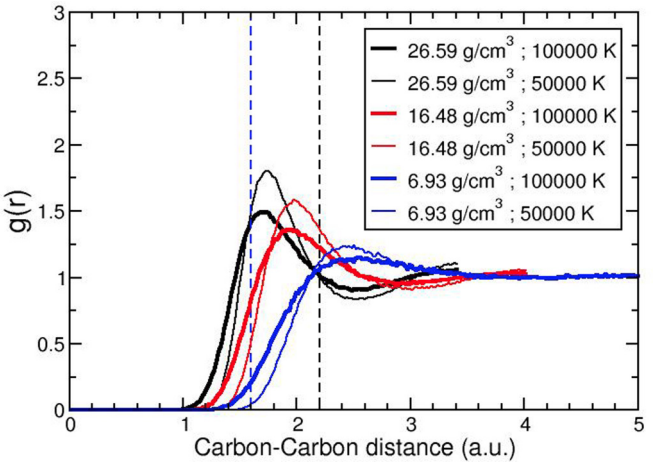

FIG. 2. (Color online) Pair correlation function for high-pressure liquid carbon for $T = 50\,000$ K and 100 000 K from PBE-DFT-MD. The black and blue dashed vertical lines are the diameter of the 1.1 and 0.8 bohr PAW potentials, respectively.

valence. For all cases tested, we find that a 5442 eV plane-wave cutoff energy is enough to reach convergence. For the PAW test, we use fcc cells with lattice constants chosen so that the carbon-carbon nearest neighbor distances are representative of the distances observed during the highest-P and highest-T DFT-MD runs. These tests are performed with the QUANTUM ESPRESSO (QE) package [28]. Figure 3 shows a comparison of the pressure obtained for this fcc cold curve with the different PAWs (for both VASP and QE). Note that two different $r_{\rm cut} =$ 1.1 bohrs and three different $r_{\rm cut} = 0.8$ bohrs are compared; for the latter choice, three different variants of PAW are used, two of which have all 6 electrons treated as valence. We only observe appreciable deviations between the different PAWs

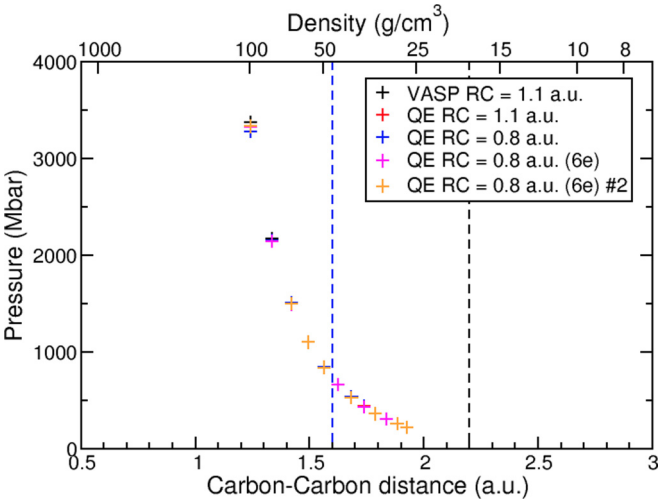

FIG. 3. (Color online) Pressure (at $T = 0$ and for fixed ionic positions) versus interionic distance for fcc carbon with various PAW potentials using PBE-DFT. The black and blue dashed vertical lines are the diameters of the 1.1 and 0.8 bohr radius PAW potentials, respectively. QE indicates that the PAW potentials and resulting cold pressures were constructed using the QUANTUM ESPRESSO package [28].

for densities above 60 g/cc, corresponding to carbon-carbon distances of ∼1.3 bohrs (0.7 Å). The difference in the calculated pressure between the VASP $R_{\rm cut} = 1.1$ bohrs PAW potential and the 6 electron PAW is only 1% up to densities of 100 g/cc. This corresponds to carbon-carbon distances of 1.1 bohrs which is essentially the smallest carbon-carbon distances sampled during the highest temperature and highest density MD runs. However, this is no guarantee that the dynamics are not affected by the overlapping PAW spheres. In this sense, we submit that our DFT-MD EOS data for the very highest densities and temperatures reported here may be of slightly lower accuracy than those for the more moderate conditions. Nevertheless, we stress that the bulk of our conclusions below should be unaffected by this fact.

Another altogether different approach to treating this problem is to dispense with the use of pseudopotentials completely and use all-electron methods, such as full-potential linear augmented plane wave (LAPW), augmented plane wave plus local orbital (APW+lo), or linear muffin-tin orbital (LMTO) schemes. This way, the frozen-core approximation inherent even in the typical use of PAWs can in principle be eliminated. We have used the all-electron full-potential APW+lo method as implemented in WIEN2K [29] to compute volume-dependent pressures of the fcc phase of carbon, in order to compare to our PAW results. The smallest fcc unit cell parameter was $a = 1.6a_0$ corresponding to an interatomic distance of $1.13a_0$. For that reason an unusually small sphere radius of 0.55 bohrs was used for C. At these small distances the 1*s* electron can no longer be considered as a core electron; it was included in the valence band and treated as semicore with a local orbital (LO) basis. For the 2*s* and 2*p* orbitals, APW+lo bases were used. As expected, the major electronic effect of such high atomic densities is a very large dispersion of the bands. In particular, we computed the carbon 1*s* orbital bandwidth to be ∼88 eV at the highest compression studied. Results for the fcc cold curve are shown in Fig. 4. Note the exceptionally small volumes and high pressures here. We find the results of the two methods to be practically indistinguishable; differences are better than one part in 1000 for the pressure. We are therefore confident that our cold compressibilities of carbon using the PAW framework are sufficiently accurate for our purposes here. Also shown are comparisons to two spherical average atom-in-jellium approaches: Thomas-Fermi [12] and Purgatorio [30] (Kohn-Sham DFT atom-in-jellium); both are discussed below in conjunction with the modeling of electronic excitations in the high-T liquid. From this we see that the DFT cold curve in the ultrahigh-pressure regime is well described by a theory which possesses atomic shell structure (Purgatorio) but lacks a description of directional bonding. Though the Thomas-Fermi result is substantially stiffer, gradient and correlation corrections to Thomas-Fermi are expected to correct this to a large degree [7].

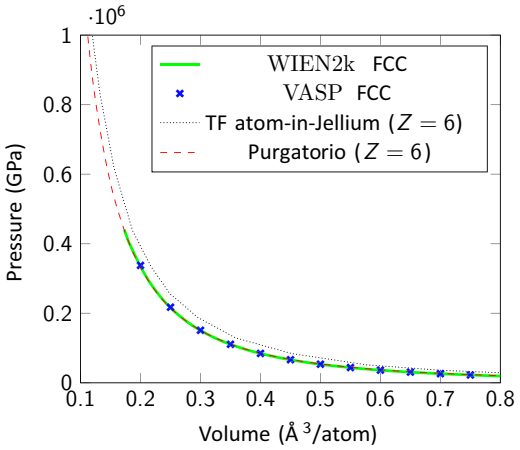

FIG. 4. (Color online) Cold compression curves for fcc carbon as computed by PBE-GGA DFT using two different computational prescriptions: PAW pseudopotentials with the VASP (plane-wave basis) code (blue points), and all-electron full-potential calculations with LAPW and APW+lo bases as implemented in the WIEN2K code (green curve). Average-atom Thomas-Fermi [12] (black dashed curve) and average-atom Kohn-Sham DFT (Purgatorio [30]; red dashed curve) are shown for comparison. Note that the highest-pressure point obtained with the all-electron code is at $P \sim 3.5\times10^5$ GPa = 3500 Mbar, more than an order of magnitude higher than the highest pressures under consideration in the EOS model of this work. Though not apparent in the figure, the largest deviation between all-electron and PAW results throughout this range is <0.1% in pressure.

B. PIMC calculations

In order to investigate the EOS of C for temperatures well above 100 000 K (which is the highest T with which we used DFT-MD), we employ the path integral Monte Carlo (PIMC) method. PIMC is the most accurate and efficient first-principles simulation technique to study the equilibrium properties of quantum systems in high-temperature plasma states. Fermionic PIMC simulations have been applied to study hydrogen [31–39], helium [40,41], hydrogen-helium mixtures [42], and one-component plasmas [43,44], and most recently to simulate carbon and water plasmas [14]. In PIMC simulations, electrons and nuclei are treated equally as Feynman paths in a stochastic framework for solving the full, finite-temperature, quantum many-body problem. The natural operator to work within this context is the thermal density matrix represented as a path integral in real space,

$$\begin{aligned}\rho(\mathbf{R},\mathbf{R}';\beta) &\equiv \langle \mathbf{R}|e^{-\beta\hat{\mathcal{H}}}|\mathbf{R}'\rangle \\ &= \int\cdots\int d\mathbf{R}_1\, d\mathbf{R}_2\, \ldots\, d\mathbf{R}_{M-1}\, \rho(\mathbf{R},\mathbf{R}_1;\Delta\tau) \\ &\quad \times \rho(\mathbf{R}_1,\mathbf{R}_2;\Delta\tau)\ldots\rho(\mathbf{R}_{M-1},\mathbf{R}';\Delta\tau) \\ &= \int_{\mathbf{R}\to\mathbf{R}'} \mathcal{D}\mathbf{R}(\tau)\exp\{-S[\mathbf{R}(\tau)]\}, \end{aligned} \tag{1}$$

where $\mathcal{H}$ is a many-body Hamiltonian, $\beta = 1/k_BT$ assumes the role of imaginary time, $\mathbf{R} = (\mathbf{r}_1,\mathbf{r}_2,\ldots\mathbf{r}_N)$, $\mathbf{r}_i$ is the position of the ith particle, M is the number of time slices, and $\Delta\tau = \beta/M$ is the step size in imaginary time intervals. $S[\mathbf{R}(\tau)]$ is the action, which determines the weight of every path. The kinetic energy operator controls the diffusion of the paths in imaginary time and keeps bead $\mathbf{R}_i$ at adjacent time slices close together. A thermodynamic function corresponding to an operator $\hat{\mathcal{O}}$ can be derived from $\langle\hat{\mathcal{O}}\rangle = \mathrm{Tr}(\hat{\rho}\hat{\mathcal{O}})/Z_c$, where $Z_c = \mathrm{Tr}(\hat{\rho})$ is the canonical partition function.

PIMC explicitly addresses all the physics of high-T plasmas including effects of bonding, ionization, exchange correlation, and quantum degeneracy on an equal footing, and thereby circumvents both the need to occupy single-particle states and the need to employ exchange-correlation approximations inherent in DFT. The Coulomb interaction between electrons and nuclei is introduced using pair density matrices derived using the eigenstates of the two-body Coulomb problem [45]. The periodic images are treated using an optimized Ewald breakup [31,46] applied to the pair action [13].

Challenges with the PIMC formalism arise in fermionic simulations because only antisymmetric eigenstates contribute to the partition function. Those can be projected out by introducing an additional sum over all permutations, $\rho_F(\mathbf{R},\mathbf{R}',\beta) = 1/N!\sum_{\mathcal{P}}(-1)^{\mathcal{P}}\rho(\mathbf{R},\mathcal{P}\mathbf{R}',\beta)$. Straightforward integration methods all lead to unstable algorithms due to the *fermion sign problem*, which is the result of the near complete cancellation of positive and negative contributions to the many-body density matrix.

A fixed-node approximation [47,48] was initially introduced to solve the sign problem for ground-state quantum Monte Carlo calculations. For the finite-temperature PIMC simulation, a restricted-path method was developed [49], where one only integrates over all paths that do not cross the nodes of a *trial* density matrix, $\rho_T(\mathbf{R},\mathbf{R}';\beta)$, which must be available in analytic form. The fermionic version of Eq. (1) then reads

$$\rho_F(\mathbf{R},\mathbf{R}';\beta) = \frac{1}{N!}\sum_{\mathcal{P}}(-1)^{\mathcal{P}}\int_{\rho_T(\mathbf{R}(\tau),\mathbf{R}';\tau))>0}^{\mathbf{R}\to\mathcal{P}\mathbf{R}'}\mathcal{D}\mathbf{R}(\tau) \times \exp\{-S[\mathbf{R}(\tau)]\}. \quad (2)$$

In addition to weighting all paths according to their action and summing over permutations, one must also check whether the sign of the trial density matrix has remained positive during every Monte Carlo move. If a sign change occurs anywhere along the new path, the proposed move is rejected. The $\mathbf{R}'$ argument in the nodal restriction plays a special role because the sign of the trial density matrix at all other time slices depends on it.

The restricted-path method provides the exact answer if the nodes from the exact many-body density matrix are used. Since exact nodes are not known for interacting systems, one must work with approximate nodes. However, within any given set of nodes, the restricted path method will obtain the best possible solution that includes all interaction and correlation effects. The PIMC method used here employs a free-particle nodal structure, which has been shown to be sufficient for carbon at temperatures where atoms still have occupied 1s states but partially occupied 2s states ($T \geqslant 2.5\times10^5$ K) [14].

Using the restricted-path, free-particle nodal framework, we use all-electron PIMC to compute equations of state for carbon at densities of 0.1, 3.18, 8.5, and 11.18 g cm^{-3} over a temperature range of 10^5–10^9 K (though we present data pertaining to all four isochores in the Supplemental Material [19], we stress that 0.1 g/cc is below the low-density limit of applicability of the EOS model described below) [50]. A sufficiently small time step associated with PIMC path slices is determined by converging total energy as a function of time step until it changes by less than 0.2%. We use a time step of 0.0078125 Ha^{-1} for temperatures below 5×10^6 K and, for higher temperatures, the time step decreases as $1/T$ while keeping at least four time slices in the path integral. In order to minimize finite-size errors, the total energy was converged to better than 0.2% for a 24 atom cubic cell. Though this may seem like a small number of atoms, we stress that the number of atoms/cell needed to accurately compute energy and pressure decreases rapidly for condensed systems as T is increased into the plasma regime [14,34,51].

III. CONSTRUCTION AND DISCUSSION OF EOS MODEL

Because the primary aim of this work is to construct an accurate wide-ranging EOS model for carbon, we must fit the discrete EOS data points obtained from our DFT-MD and PIMC simulations by an underlying free energy model. The model we choose is necessarily approximate (because an exact analytic form for the free energy of a many-body system is impossible to obtain), but it is important to stress that the approximations inherent in its construction, which we now discuss, are not imposed on the underlying *ab initio* data themselves. Whenever possible, we let these data guide us in determining the specific forms of the free energy models that we use. The use of a specific, though approximate, underlying global free energy model is needed in order to provide an EOS which is smooth and which respects the conditions of thermodynamic consistency and stability [52], as well as the proper limiting behavior (ideal gas at high T, low ρ, etc.).

We make the fundamental assumption that the Helmholtz free enegy, $F = E - TS$, of each phase can be decomposed into the following terms:

$$F(V,T) = E_{\rm cold}(V) + F_{\rm ion}(V,T) + F_{\rm elec}(V,T), \quad (3)$$

where $F_{\rm ion}$ and $F_{\rm elec}$ represent the contributions from ionic and electronic excitations, respectively. While the identification of a temperature-independent piece ($E_{\rm cold}$) is always possible by virtue of the fact that it is merely definitional, the separation of the thermal part into decoupled ionic and electronic pieces is a major assumption. In a practical sense, this assumption is at least a reasonable starting point since for solids at lower T, it has been shown to be accurate when comparing to DFT-MD data [9,53,54], and for the liquid at very high temperature (ideal gas limit) it is also trivially satisfied because interactions between particles are of no importance. It is not necessarily justified for intermediate temperatures, but we shall invoke the approximation knowing that the *ab initio* EOS data to which we fit (obtained from DFT-MD and PIMC) do not result from making this assumption. We will see below that appropriate choices of the terms in Eq. (3) provide an excellent fit to our DFT-MD and PIMC EOS data, while exhibiting the appropriate limits.

A. Solid phases

For the solid phases we consider, diamond, BC8, simple cubic (sc), and simple hexagonal (sh), we take $E_{\rm cold}(V)$ to be the internal energy of the perfect crystalline lattice (with motionless ions) at $T = 0$ [18] with the electrons in their ground state. We find that our DFT data for the internal energy of the perfect lattice for the various phases throughout our

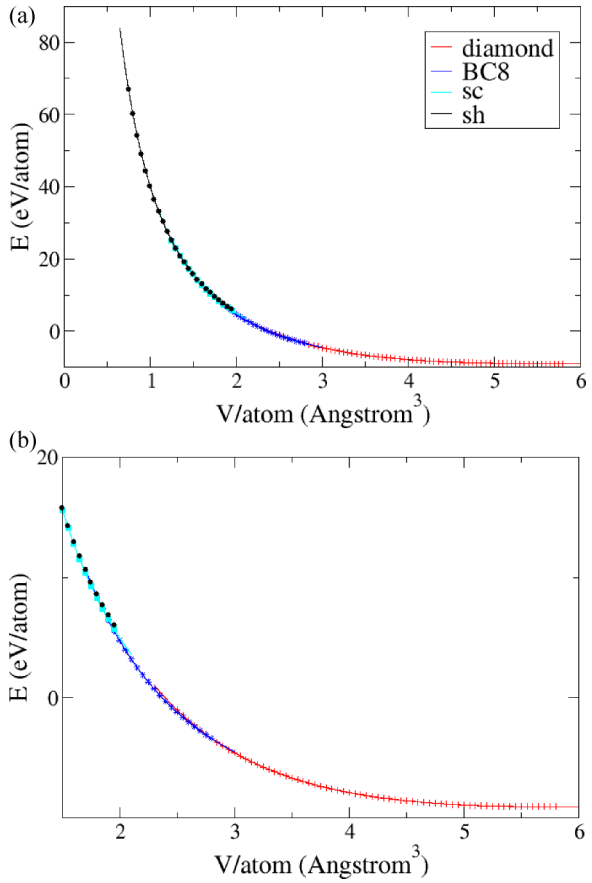

FIG. 5. (Color online) Internal energy at $T = 0$ (and for fixed ions) in eV/atom versus V/atom in Å^3 for various phases of C. Points indicate the results of PBE-DFT calculations, while the thin curves are fits to these data used in our EOS model. The phases represented are diamond (red), BC8 (blue), sc (cyan), and sh (black). (a) shows the whole range over which the EOS model is constructed, while (b) shows a closer view of the range between $V = 2$ and 5 Å^3/atom.

range of interest is fitted extremely well by the Vinet equation of state [55],

$$E_{\rm cold}(V) = \phi_0 + \frac{4V_0B_0}{(B'-1)^2}[1-(1+X)\exp(-X)],$$

where

$$X = \frac{3}{2}(B'-1)[(V/V_0)^{1/3}-1]. \quad (4)$$

Here, B_0 is the bulk modulus at the volume V_0, B' is the pressure derivative of the bulk modulus at V_0, and ϕ_0 is the internal energy at V_0. Figure 5 shows the computed cold curves, $E_{\rm cold}(V)$, of the various phases, together with our fits to them, using Eq. (4). The cold curve parameters for each phase (ϕ_0, B_0, B', and V_0) are given in Table I, along with the other phase-dependent parameters we discuss below. Our DFT results using the Perdew-Burke-Ernzerhof (PBE) GGA exchange-correlation functional for the solid cold curves are very similar to those of Ref. [15], but there are differences which result presumably from the use of different pseudopotentials and associated choices for the plane wave energy cutoff in the determination of the internal energy.

TABLE I. Phase-dependent EOS model parameters for the solid phases of our multiphase C EOS. The upper segment of the table concerns cold curve parameters, the middle segment quasi-harmonic ion-thermal parameters, and the lower segment electron-thermal/anharmonic-ion-thermal parameters. All volumes (V) are in Å^3/atom, B_0 is in GPa, B' is unitless, ϕ_0 is in eV/atom, all characteristic temperatures (θ) are in kelvins, A parameters are in Å^{-3}, B parameters are unitless, α_0 is in kelvin^{-1}, and κ is unitless.

Parameter	Diamond	BC8	sc	sh
V_0	5.7034	6.242	7.9899	9.6061
B_0	432.4	221.2	59.09	22.12
B'	3.793	4.697	5.763	6.495
ϕ_0	−9.066	−8.705	−7.525	−6.5
V_p	5.571	3.176	2.658	1.35
θ_A^0	1887.8	1961.9	2089.8	4183.8
A_A	−0.316	0.0	0.0	0.4354
B_A	0.913	0.0	0.212	0.4034
θ_B^0	1887.8	3176.3	2961.3	4183.8
A_B	0.168	0.156	0.0	0.4354
B_B	0.429	0.532	0.817	0.4034
θ_1^0	1887.8	2800.6	2328.3	4183.8
A_1	0.0846	0.112	0.369	0.4354
B_1	0.499	0.449	0.302	0.4034
V_e	5.785	5.077	1.0	1.0
α_0	3.79×10^{-5}	5.5×10^{-5}	1.37×10^{-5}	1.58×10^{-5}
κ	0.0	0.0	0.637	0.81

Though small, these differences give rise to rather pronounced changes in the predicted phase transition pressures (BC8 → sc → sh) when compared to the phase diagram presented in Ref. [15]. This will be discussed more below, after the thermal components of the free energies are considered and our phase diagram is presented. At this point, we note that we have checked that our inferred transition pressures at $T = 0$, determined from the two-phase Maxwell construction [52], should be inaccurate by no more than a few percent due to our use of the Vinet fitting form, Eq. (4) (though we in no way imply that PBE GGA-DFT is necessarily this accurate for predicting these transition pressures at such high compressions).

Because small changes in $E_{\rm cold}(V)$ for each phase can greatly affect the positions of phase lines, it is desirable to investigate the sensitivity of our results to changes in the choice of the DFT exchange-correlation functional. This is especially of interest in light of recent work on high-pressure hydrogen [56] and high-pressure water [57] in which the phase transition pressures between solid phases were shown to change significantly when replacing the PBE GGA functional by a so-called van der Waals functional which has a different treatment of exchange and correlation. To study this for our solid carbon phases, we have computed the cold energies and pressures using the functional of K. Lee *et al.* [23], based on the PW86 GGA exchange [58], with a computational prescription otherwise identical to that used for our PBE calculations (in terms of numbers of k points, etc.). We find, for all four solid phases under consideration here, only a tiny and practically negligible dependence of the cold energies and pressures on this change. We therefore see that for C in

the conditions we consider (pressures up to 14 000 GPa), the PBE functional and the functional of Ref. [23] give essentially the same results for all practical purposes. We attribute this at least in part to the fact that high-density carbon is not a molecular system like the high-pressure phases of H studied in Ref. [56]. In addition, hydrogen may well be the exception rather than the rule: The spatially averaged reduced density gradient, $s = \frac{|\nabla\rho|}{2(3\pi^2)^{1/3}\rho^{4/3}}$, and its variation between molecular and atomic species, is much larger for hydrogen than it is in other systems (e.g., silicon, lithium fluoride, and nitrogen; see Table I in Ref. [59]). Only in systems where $\langle s\rangle$ is large and changes in $\langle s\rangle$ between competing phases are appreciable would the differences between these exchange-correlation functionals be manifest.

We build the phase-dependent $F_{\rm ion}(V,T)$ for the solid phases from our DFT calculations of phonon densities of states at a large collection of volumes. These phonon densities of states are computed assuming zero electron temperature, so the ion excitation energies are constructed for cases in which the electrons are in their instantaneous ground state (for each ionic configuration). From this information, we use the quasiharmonic approximation [52] to produce $F_{\rm ion}(V,T)$. Though this $T_{\rm electron} = 0$ quasiharmonic treatment might seem suspect at high T, it has long been known to produce a very accurate rendering of the EOS of many materials even at temperatures approaching $T_{\rm melt}$ [52]. This was shown in particular for C in our earlier work on the diamond and BC8 phases [9]. Moreover, this has been shown to be true even for good metals such as gold [60]. In our present case, the (high-pressure portion of) BC8, sc, and sh phases are metallic, but with fairly low densities of electronic states at the Fermi level. We therefore expect the standard quasiharmonic treatment with phonon densities of states computed at $T_{\rm electron} = 0$ to be quite accurate, and demonstrate so for diamond by comparing to DFT-MD data for temperatures as high as $T \sim T_{\rm melt}$ (see the discussion surrounding Fig. 7).

Since we must extract smooth volume dependencies of the phonon densities of states for each phase, $D_V(E)$, in order to compute the ionic contributions to the pressure, we represent $D_V(E)$ by the minimal number of energy moments needed to describe the resulting $F_{\rm ion}(V,T)$ with sufficient accuracy. These V-dependent moments of $D_V(E)$ for a given phase are the phase-dependent Debye temperatures. As discussed in Ref. [9], it is necessary to represent diamond and BC8 phases by *two* such Debye temperatures for each V, due to the bimodal nature of the diamond and BC8 $D_V(E)$ under compression. We choose to adopt this framework for the sc phase as well, but not for the sh phase. The reason is that our DFT calculations of the phonon densities of states of the sh phase show them to be quite similar to those of a perfect Debye model [$D_V(E) \propto E^2$ for $E \leqslant \theta$ and 0 for $E > \theta$] throughout the range of V we consider. The quantitative measure which determines this similarity is the near-equality of the low-order energy moments of $D_V(E)$ for each V. Figure 6 shows the three moments [52], $k_{\rm B}\theta_0(V) = e^{1/3}\exp[\int_0^\infty d\varepsilon\,\ln(\varepsilon)D_V(\varepsilon)]$, $k_{\rm B}\theta_1(V) = 4/3\int_0^\infty d\varepsilon\varepsilon D_V(\varepsilon)$, and $k_{\rm B}\theta_2(V) = \sqrt{\frac{5}{3}\int\varepsilon^2 D_V(\varepsilon)d\varepsilon}$, as functions of V for BC8, sc, and sh phases as computed by DFT linear response methods. While the BC8 and sc phases show θ_0, θ_1, and θ_2 to be increasingly unequal as V is decreased, they remain very close for all V for the sh phase. We therefore use a conventional Debye model (with Debye temperature equal to θ_0) for sh and double-Debye models (as introduced and discussed in Ref. [9]) for diamond, BC8, and sc phases. We add in passing that we have additionally shown that the phonon moments of the sc phase are sufficiently close that this phase too can be treated with a conventional single-Debye model without significant loss of accuracy.

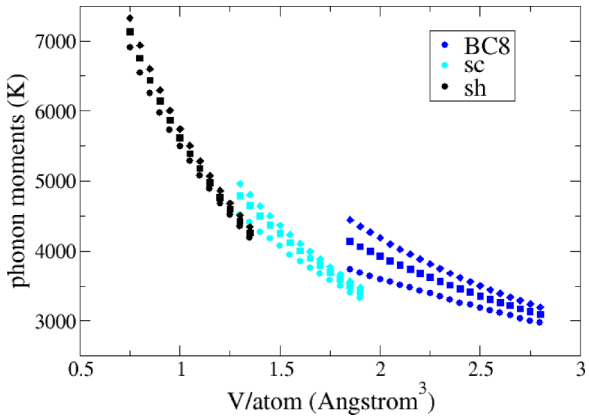

FIG. 6. (Color online) Moments of the phonon densities of states θ_0 (circles), θ_1 (squares), θ_2 (diamonds) in kelvins versus V/atom in Å^3 for BC8 (blue), sc (cyan), and sh (black) phases as computed with linear response methods using PBE-DFT.

The free energy for the double-Debye model is written as [61]

$$F_{\rm ion}(V,T) = \left[\frac{\theta_{\rm B}(V)-\theta_1(V)}{\theta_{\rm B}(V)-\theta_A(V)}\right]F_{\rm A}(V,T) + \left[\frac{\theta_1(V)-\theta_{\rm A}(V)}{\theta_{\rm B}(V)-\theta_{\rm A}(V)}\right]F_{\rm B}(V,T), \quad (5)$$

where $F_{\rm A}$ and $F_{\rm B}$ are the single-Debye free energies for the individual peaks [9], labeled A and B, associated with a given phonon density of states, $D_V(E)$. Here, $\theta_1(V)$ is the first energy moment of $D_V(E)$ as defined above. The Debye temperatures for the individual peaks, $\theta_{\rm A}$ and $\theta_{\rm B}$, are related to the moments θ_0, θ_1, and θ_2 by Eqs. (10)–(12) in Ref. [9]. In this way, the functions $\theta_{\rm A}(V)$, $\theta_{\rm B}(V)$, and $\theta_1(V)$ for each phase are computed from the $D_V(E)$. For all such functions for the various phases, we find that they are fitted very accurately by the functional form

$$\theta(V) = \theta^0\left(\frac{V}{V_p}\right)^{-B}\exp[A(V_p - V)], \quad (6)$$

where θ^0 is the value at a reference volume V_p. This is consistent with the assumption that the ion-thermal Grüneisen parameter for $\theta(V)$ is equal to $\gamma = AV + B$ [9,54]. These phase-dependent ion excitation free energy parameters, as determined from our DFT calculations of the phonon densities of states, are displayed in Table I.

We investigated anharmonicity for diamond and BC8 phases in Ref. [9] by comparing E and P from our DFT-derived quasiharmonic model with E and P from DFT-MD. It was shown that throughout the range of stability of the

diamond and BC8 phases, the addition of a term of the form $F_{\rm anh}(T) = -\alpha T^2/2$, with α independent of V, was sufficient to bring the model results into accord with DFT-MD. Because no substantive V dependence to this correction was found, only E and not P was altered by this addition. Furthermore, the smallness of the inferred coefficient α produced only very minor changes to the internal energies of the diamond and BC8 phases. We include those same anharmonic free energy terms in our current model, mostly to maintain consistency with our previous work; however, we have not yet conducted a similar study for the sc or sh phases. Thus, we refrain from including a small anharmonic contribution to those phases. The precise quantitative effects of anharmonicity in sc and sh await further study.

The electronic excitation term for each solid phase, $F_{\rm elec}(V,T)$, is taken be of the form

$$F_{\rm elec}(V,T) = -\tfrac{1}{2}\alpha(V)T^2 k_{\rm B}/{\rm atom}, \qquad (7)$$

which is motivated by a performing a Sommerfeld expansion of the electronic excitation free energy, assuming $T/T_{\rm Fermi}$ to be a small parameter [52]. This contribution is extracted from PBE GGA-DFT calculations in which electronic occupancies are constrained by a Fermi-Dirac distribution with temperature T, but for ions *fixed* in their lattice positions. As discussed in Ref. [9], this term is essentially zero for the diamond phase throughout its stability field, and is exceedingly small (though nonzero) for the BC8 phase as well [62]. For this reason, electronic excitation contributions were intentionally neglected by those authors in their solid-phase EOS models. Here we choose to include these terms for the sc and sh phases; their values for sc and sh are somewhat larger than those of BC8, because the electronic density of states near $E_{\rm Fermi}$ generally increases with compression. Still, we find that their inclusion has an exceedingly small effect on the EOS and the resulting phase lines, as also noted in the work of Ref. [15]. We determine that these small DFT-derived contributions are accurately represented by the expression of Eq. (7) with $\alpha(V) = \alpha_0(V/V_e)^\kappa$ [9,52,54]; our choices for α_0, κ, and V_e are presented in Table I for each phase. Note that the nonzero values for α_0 which appear for the diamond and BC8 phases in this table pertain to the anharmonic ion-thermal free energy contributions (see above), and are *not* due to electronic excitations [63].

In order to check the validity of our solid-phase EOS model for C, we compare to our DFT-MD results for pressure and internal energy in the diamond phase throughout a dense grid of volumes and temperatures (individual comparisons for the sc and sh phases are discussed below as well). These results exist throughout a range where diamond is predicted to be the stable phase (3.0 Å^3/atom $< V <$ 5.6 Å^3/atom, and 2000 K $< T <$ 9000 K). Figure 7 shows that the model agrees with the diamond-phase DFT-MD quite well, even though these MD data, per se, were not used in the fitting (rather, only cold curves, PDOSs, and electronic DOSs were used—with the exception of the very small anharmonic terms determined in Ref. [9]).

Since the sc and sh phases are metallic, it is of interest to check the validity of the $F = F_{\rm cold}$ + (quasiharmonic) $F_{\rm ion}$ + $F_{\rm elec}$ assumption by comparing directly to DFT-MD, just as we have for the diamond phase (Fig. 6). At the points

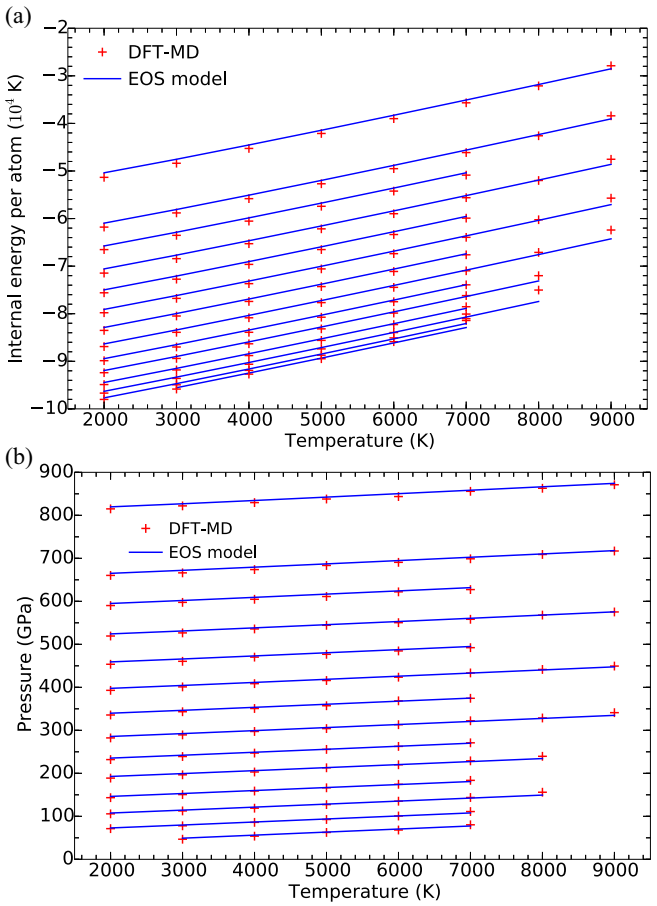

FIG. 7. (Color online) (a) Internal energy (K/atom) isochores versus T (K) for the diamond phase. (b) Pressure (GPa) isochores versus T (K) for the diamond phase. Red points are the results of DFT-MD; blue lines are the results of our EOS model. In both plots, V ranges from 3.0683 Å^3/atom to 5.3903 Å^3/atom.

(sc) (V = 1.5 Å^3/atom, T = 5800 K), (V = 1.7 Å^3/atom, T = 5800 K) and (sh) (V = 1.0 Å^3/atom, T = 7500 K), (V = 1.35 Å^3/atom, T = 7500 K), chosen so that T is well above the Debye temperatures at these V, we find that our DFT-MD pressures are a few tenths of a percent different from the pressures of our model. This is identical to the level of agreement shown in Fig. 6. We add that the computations of the relevant moments of the PDOSs themselves (as shown in Fig. 5) are also very insensitive to $T_{\rm electron}$ for these phases. For instance, we find that the resulting phonon moments for sh throughout its stability field change by no more than ∼1% from those of Fig. 5 when $T_{\rm electron}$ is chosen to be 7500 K. These findings reflect the fact that these carbon phases, while metallic, do not possess large, sharp peaks in their densities of electronic states in the neighborhood of the Fermi level [64]. As a final illustration of this insensitivity, Fig. 8(a) shows the PDOSs, self-consistently determined from linear response using Mermin-DFT, for six electron temperatures between 0 K and 6000 K for V= 1.35 Å^3/atom (sh phase). The various curves are extremely similar. Figure 8(b) shows the resulting quasiharmonic ion-thermal free energy as computed at each T from these T-dependent PDOSs (blue points); agreement with the ion-thermal free energy of our EOS model

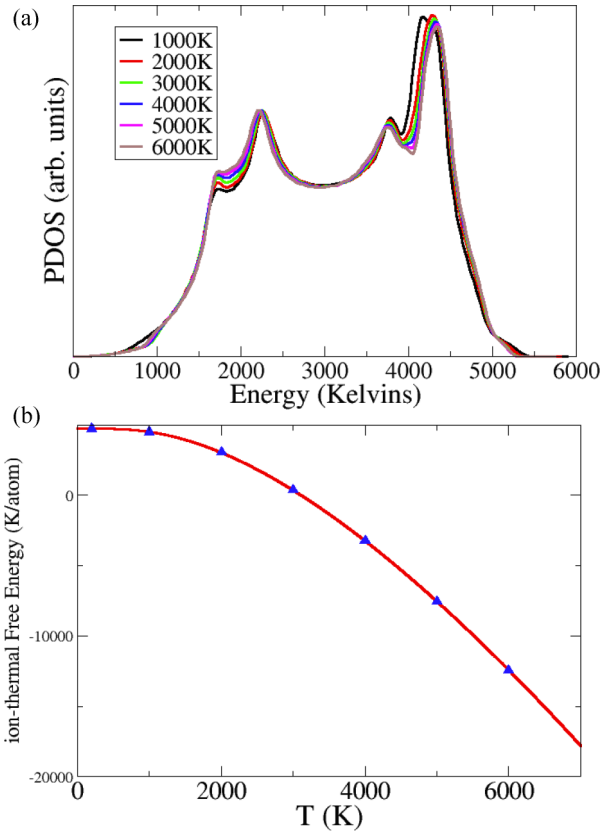

FIG. 8. (Color online) (a) Phonon densities of states (PDOSs) of sh-phase carbon at $V = 1.35$ Å^3/atom as computed with PBE-GGA DFT using the Mermin formulation at various electron temperatures, indicated in the legend. (b) Quasiharmonic ion-thermal Helmholtz free energy [52] computed with the above PDOSs (plus an additional PDOS not shown above, for $T_{\text{electron}} = 200$ K) at each corresponding temperature (blue) points, together with the ion-thermal free energy for our EOS model (red curve), constructed using (1) the low-T PDOS at this V and (2) a Debye approximation to the full quasiharmonic free energy (see text).

(red curve) demonstrates both the efficacy of the $T_{\text{electron}} = 0$ approximation (used to construct the model) and the suitability of the Debye approximation in its description of the full quasiharmonic free energy. Comparisons for other V and for the other metallic phase in our range of interest, sc, yield similar results. Thus, our strategy of using the $T_{\text{electron}} = 0$ phonon densities of states to construct F_{ion} is sufficiently accurate for our purposes.

The striking agreement described above illustrates the suitability of our $F = E_{\text{cold}} + F_{\text{ion}} + F_{\text{elec}}$ prescription, together with the individual models for these DFT-derived terms, as described by Eqs. (4)–(7). In this sense, we are confident that our phase-dependent EOS model for solid C throughout the range of our interest ($0 < P < 14\,000$ GPa) is consistent with the (PBE) GGA-DFT prediction of the EOS. It is a separate question as to the degree of accuracy of GGA-DFT itself in predicting the EOS of these solid C phases. While an investigation of alternate means of producing first-principles predictions of solid-phase equations of state are outside the scope of this work, we do employ both GGA-DFT and the entirely unrelated theory, PIMC, to predict the liquid C EOS. As will be shown in the next section, detailed features of the T-dependent specific heat of the liquid (which were entirely unexpected by us, prior to this work) are shown to arise from both theories, lending further credence to the efficacy of Born-Oppenheimer Mermin-formulation GGA-DFT for carbon EOS prediction.

B. Liquid phase

As demonstrated in numerous classical and DFT-MD investigations on the EOS of liquids [9,54,65–67], the equation of state of a monatomic liquid in the neighborhood of its melt curve is strikingly similar to that of a solid, in the sense that its specific heat at constant V is very nearly independent of V and is equal to $\sim 3k_{\text{B}}$/atom. Indeed, we observed this for C in our earlier work, even for temperatures up to twice T_{melt} over a wide range of compressions [9,68]. For this reason, it is justified to assume that the paradigm of Eq. (3) is a reasonable starting point for the construction of a free energy model with which to fit our DFT-MD results. It is, however, important to point out that there is no natural way to determine the E_{cold}, F_{ion}, and F_{elec} terms independently, because the liquid cannot be described as a perturbation away from a fixed configuration of ions. Still, we submit that our (and others') previous successes in constructing EOS models for liquids (and for C in particular) based on this paradigm suggests that this is a fruitful strategy for creating a thermodynamically consistent EOS model in good agreement with *ab initio* data. And just as for the solid phases discussed above, our justification of the adoption of this strategy will come from our demonstration that the agreement with such data is in fact satisfactory, though we shall see below that in the case of the liquid (Figs. 11, 12, and 13), the agreement is not quite as favorable as for the diamond comparison shown in Fig. 7. Finally, we stress once again that the approximations inherent in the construction of the EOS model are not imposed on the data (DFT-MD and PIMC) themselves.

The specific models we use for the terms in Eq. (3) for the liquid are similar to those assumed in Ref. [9], though with some important differences which result from our consideration of higher P and higher T in the present work. In this approach, the cold piece is once again taken to be of the Vinet form [55] [Eq. (4)], though augmented with a few so-called break points which introduce bends in $E_{\text{cold}}(V)$ over localized regions in V [9,69]; additional bends at small V are included to improve agreement with our liquid DFT-MD data performed at densities far higher than those considered in the work of Ref. [9]. The ion-thermal term at lower T (up to $\sim$ twice T_{melt}) is treated in the scheme of Chisolm and Wallace [65], which is an effective Mie-Grüneisen model for the liquid with a V-dependent characteristic temperature, $\theta(V)$, which we again take to have the form of Eq. (6). This model was used before for liquid C [9], and is constrained to have an ion-thermal specific heat, $C_V^{\text{ion}} = 3k_{\text{B}}$/atom; this was mandated by the fact that the ($T < 20\,000$ K) DFT-MD data exhibited $C_V^{\text{total}} \sim 3k_{\text{B}}$/atom while it was also demonstrated that the effects of electronic excitation in the low-T liquid were of negligible importance (thus, $C_V^{\text{elec}} \sim 0$) [9]. Our new DFT-MD data show identical behavior throughout the wider range of V considered here.

At temperatures well above $2T_{\rm melt}$ (for the V of interest here), two additional pieces of physics are known to enter which necessarily change the picture relative to that seen at lower T: (1) Electronic ionization becomes important (particularly at much higher T and/or ρ in the C plasma). At sufficiently high T, all 6 C electrons are ionized and contribute $6\times 3k_{\rm B}/2$/atom to the total C_V. The precise manner in which ionization occurs depends on V. (2) The C nuclei themselves become more free-particle-like as T is raised, eventually contributing an additional $3k_{\rm B}/2$/atom to C_V. Because the DFT-MD results for C show that the breakdown of C_V into $C_V^{\rm ion}+C_V^{\rm elec}$ (~ 0) is reasonable at low T, and that at high T, basic physics dictates once again that $C_V = C_V^{\rm ion}+C_V^{\rm elec}$ (since for $T\to\infty$, interparticle interactions are of no importance), we deem it sensible to adopt the $F = E_{\rm cold}+F_{\rm ion}+F_{\rm elec}$ assumption for our liquid EOS model throughout the entire range of T. The natural choice for $F_{\rm elec}$ throughout this wide range is an atom-in-jellium approach in which a C ion is placed in a neutral cell embedded in a uniform electron gas of the appropriate density (specified by the choice of V). Such average-atom models have a long history in the construction of equations of state for materials over wide ranges of compression and temperature [12,17,70]. The variant we used for our work of Ref. [9] was average-atom Thomas-Fermi. This is expected to be less accurate than that of an average DFT C atom embedded in jellium since Thomas-Fermi lacks a detailed description of atomic shells. The average-atom DFT model known as PURGATORIO [30], as well as other DFT-based average-atom models [71], have been used extensively [54,67,72] to construct electronic-excitation contributions to high-T liquid free energies. We therefore explore the use of both average-atom Thomas-Fermi and PURGATORIO (average-atom DFT) for the liquid $F_{\rm elec}$ in this work. Regarding point 2 above, models in wide use such as the Cowan model [73] assume particular rates at which $C_V^{\rm ion}(T)$ decays from $3k_{\rm B}$/atom to $3k_{\rm B}/2$/atom as T is raised. Though the Cowan and related models were motivated by fixed classical potential MD studies, to the best of our knowledge, the precise nature of this decay has yet to be studied with either DFT-MD or PIMC for any elements heavier than H or He. Indeed, in our earlier C EOS work, T was not high enough to detect any notable deviation from $C_V = 3k_{\rm B}$/atom. In the next subsection, we consider a range of model choices for both $F_{\rm ion}$ and $F_{\rm elec}$ in order to determine what agrees best with our high-T *ab initio* liquid C data. What we find lends credence to the expectation that a DFT-based average-atom model is better than average-atom Thomas-Fermi, but also shows that the decay of $C_V^{\rm ion}$ to the ideal gas value is much faster than that assumed in the oft-used Cowan model [9,17,54,73].

1. The high-T liquid: Approach to the ideal gas

Since we now have first-principles electronic structure data (DFT-MD and PIMC) for liquid C at far higher T than we had previously [9], we are able to test various assumptions regarding the manner in which the specific heat at constant volume, C_V, evolves from its Dulong-Petit value ($3k_{\rm B}$ per atom) to the ideal gas limit ($6\times 3k_{\rm B}/2$ [electron] $+3k_{\rm B}/2$ [ion] $= 21k_{\rm B}/2$ per atom). To frame this discussion, we consider two different models for the high-T liquid ion-thermal free energy, and two different average-atom models for the liquid electron-thermal free energy. Because the DFT-MD and PIMC methods do not assume independent electron-thermal and ion-thermal pieces, we must compare the total EOS (E and P) from these *ab initio* predictions to those of the models which assume $E = E_{\rm cold}+E_{\rm ion}+E_{\rm elec}$ and $P = P_{\rm cold}+P_{\rm ion}+P_{\rm elec}$. In this way, we determine suitable choices for $F_{\rm ion}$ and $F_{\rm elec}$ to construct our liquid C EOS model, though we stress that these choices are necessarily not unique.

First we describe our two different models for the high-T behavior of $F_{\rm ion}$, which we call SLOW and FAST. As we have discussed, our DFT-MD shows that the ionic specific heat of the liquid must equal $3k_{\rm B}$/atom for T below roughly $2T_{\rm melt}$ [9]. And we know as well that as $T\to\infty$, we must recover $C_V^{\rm ion}\to 3k_{\rm B}/2$. The simplest model for $C_V^{\rm ion}$ which satisfies these constraints with a power-law decay in T is

$$C_V^{\rm ion} = \frac{3}{2}k_{\rm B}+\frac{3}{2}k_{\rm B}\left[\frac{T_{\rm M}(V)}{T}\right]^{\nu}, \tag{8}$$

where $\nu>0$, and $T_{\rm M}(V)$ is a V-dependent reference temperature which we call the matching temperature for reasons that will become clear [74]. Note that this C_V is unphysical for $T<T_{\rm M}(V)$; for this reason, we imagine that a Debye model (which has $C_V\to 0$ as $T\to 0$) [52] is used below $T=T_{\rm M}$. The free energy due to this specific heat can then be derived by integrating appropriately:

$$F_{\rm ion} = E_{\rm ion}-TS_{\rm ion} = \left[E_0+\int_{T_{\rm M}}^{T}C_V^{\rm ion}dT\right] - T\left[S_0+\int_{T_{\rm M}}^{T}\frac{C_V^{\rm ion}}{T}dT\right], \tag{9}$$

where E_0 and S_0 are the internal energy and entropy obtained from the Debye C_V, below $T_{\rm M}$. In the high-T limit, assuming $T_{\rm M}$ is significantly greater than the characteristic vibrational temperature of the liquid, $\theta(V)$, the Mie-Grüneisen expressions for these quantities can be substituted [68] in place of the more involved Debye model expressions: $E_0 = 3k_{\rm B}T$ and $S_0 = -3k_{\rm B}\ln[\theta(V)/T]+3k_{\rm B}$. These can be thought of as providing boundary conditions needed to determine $F_{\rm ion}$ from $C_V^{\rm ion}$ (two such conditions are needed, since C_V is a second derivative of the free energy). The resulting free energy is

$$F_{\rm ion} = -\frac{3}{2}\left(\frac{1+\nu}{\nu}\right)k_{\rm B}T+\frac{3}{2}k_{\rm B}\frac{T_{\rm M}^{\nu}T^{1-\nu}}{\nu(1-\nu)} -\frac{3}{2}k_{\rm B}\left(\frac{\nu}{1-\nu}\right)T_{\rm M}+3k_{\rm B}T\ln\left(\frac{\theta}{T_{\rm M}}\right) -\frac{3}{2}k_{\rm B}T\ln\left(\frac{T}{T_{\rm M}}\right). \tag{10}$$

It can be shown [17,73,68] that $T_{\rm M}(V)$ must satisfy the Lindemann criterion [75] for the ion-thermal pressure to asymptote to its ideal gas value as $T\to\infty$: $P_{\rm ion} = -\partial F_{\rm ion}/\partial V|_T \to 3k_{\rm B}T/V$. The case of $\nu = 1/3$ is the so-called Cowan model [17,73], and represents a SLOW decay of $C_V^{\rm ion}$ from $3k_{\rm B}$ to $3k_{\rm B}/2$. This model has been in wide use for modeling of the EOS of liquids [17], and was first proposed to describe high-T classical MD results with fixed interatomic potentials [76].

Faster decays can be chosen by increasing the value of ν in the above expressions. We find however, as described below, that a model of the above type possesses too slow a decay for any value of ν to accurately reproduce our DFT-MD and PIMC data for liquid carbon. Anticipating this, we choose our FAST model for $C_V^{\rm ion}$ to be of the form

$$F_{\rm ion} = 3k_{\rm B}T \ln\left(\frac{\theta}{T}\right) - k_{\rm B}T \ln\left[\mathrm{erf}\left(\sqrt{\frac{T_{\rm M}}{T}}\right) - \frac{2}{\sqrt{\pi}}\sqrt{\frac{T_{\rm M}}{T}}e^{T_{\rm M}/T}\right]. \quad (11)$$

The first term is a Mie-Grüneisen free energy exactly as that assumed in the SLOW model for $T < T_{\rm M}$. Here, the high-T correction (second term above) is an additive piece that causes the resulting $C_V^{\rm ion}$ to decay from $3k_{\rm B} \rightarrow 3k_{\rm B}/2$; the first portion of this decay (for T in the neighborhood of $T_{\rm M}$) is exponential in T rather than power law. This precise form arises from the classical expression for the partition function of a particle in a harmonic well further confined by hard-wall boundaries. A full explanation of the reasoning behind this model will be described in a subsequent work [77]. For now we note four important points: (1) The ion-thermal free energy models of Eqs. (10) (SLOW) and (11) (FAST) represent two extremes in the manner in which the ionic ideal gas limit is reached. (2) The SLOW model of ion thermodynamics has been in wide use [9,17,54,73], and is the model we would have chosen had we not possessed *ab initio* electronic structure data at sufficiently high T to test it. (3) The models themselves are only evaluated on their basis to best represent these data. (4) We need to use such models because our aim is to create a wide-range equation of state for C; the assumptions inherent in these models, however, are not imposed in any way on the *ab initio* electronic structure data.

Next we describe our two different models for $F_{\rm elec}$. In the average-atom approach [12], the liquid is represented by a single representative ion embedded within a medium consisting of an electron gas with a uniform positive compensating background. In the typical model of this type [17,30,71], the electron gas outside of a neutral cell surrounding the atom is uniform in density. The neutral cell containing the ion is taken to be spherical and with a radius equal to the Wigner-Seitz radius (or something similar). Electron charge density within the sphere, in the neighborhood of the atomic nucleus, is determined subject to the boundary conditions with the jellium background. Such a model is a natural description of a plasma, particularly at high densities, because ionization due to pressure and temperature arise naturally: As ρ and/or T increases, electron charge is forced out of the central spherical shell and into the jellium background. Though this atom-in-jellium picture is manifestly unable to describe directional chemical bonding, it has been shown that this coarse-grained picture does indeed reproduce the salient features of dense plasma EOS in sufficiently extreme conditions [51,72]. What it does not describe are features arising specifically from the simultaneous existence of multiple charge states (such as C^{+1}, C^{+2}, etc.). While seldom satisfactory for the prediction of spectra, this average-ionization state picture is quite accurate for EOS applications [51,72]. More specifically, its most natural application is to the determination of $F_{\rm elec}$, since the motion of the ion itself is not considered. In practice, the cold part of the free energy per ion of the average-atom system must be subtracted from the total to yield the associated electron-thermal contribution, $F_{\rm elec}(V,T) = F_{\rm AA}(V,T) - F_{\rm AA}(V,T=0)$, since $F_{\rm AA}(V,T=0)$ contains an incorrect bonding contribution [12,30,71]. We compare two choices in this work: average-atom Thomas-Fermi (AA-TF), and average-atom DFT (AA-DFT). In AA-TF, the basic quantity is the electron density; no single-particle orbitals are present. Thus, while an average ionization ($\bar{Z}$) can be determined, no atomic shell structure is present in the model. In AA-DFT, however, the Kohn-Sham single-particle states give rise to atomic shells which cause the degree of ionization to increase in jumps as T and/or ρ is raised (i.e., as single-particle orbitals move into the jellium continuum).

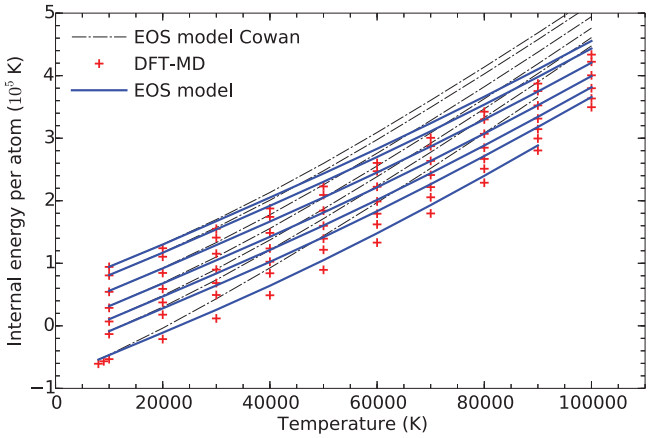

FIG. 9. (Color online) Internal energy (K/atom) isochores versus T (K) for the liquid as computed by DFT-MD (red points) and two variants of our liquid carbon EOS model: $F_{\rm ion}$ = SLOW (i.e., Cowan) model (black dashed-dotted lines), $F_{\rm ion}$ = FAST model (blue lines). V ranges from 2.05610 Å^3/atom to 5.39030 Å^3/atom. Note that this plot contains roughly one-half of the isochores in this density range for which we produced DFT-MD data.

We now compare our *ab initio* data for liquid C to EOS models constructed using all four combinations resulting from both choices of high-T ion-thermal model, and both choices of electron-thermal model: (1) $F_{\rm ion}$= SLOW, $F_{\rm elec}$= AA-DFT, (2) $F_{\rm ion}$= FAST, $F_{\rm elec}$= AA-DFT, (3) $F_{\rm ion}$= SLOW, $F_{\rm elec}$= AA-TF, (4) $F_{\rm ion}$= FAST, $F_{\rm elec}$= AA-TF. The comparisons are conducted in this fashion because the *ab initio* data to which we compare cannot be decomposed into separate ion-thermal and electron-thermal pieces.

We first illustrate the comparison between choices 1 and 2 above with respect to their agreement with our DFT-MD data. Figure 9 shows internal energy, E, versus T for liquid C on a densely spaced grid of isochores for densities 3 g/cc $< \rho <$ 12 g/cc. Red points are the results of DFT-MD extending up to T = 100 000 K as described in Sec. II A. Black dashed-dotted lines are the predictions of a liquid C EOS model for these same (ρ,T) states, which has been constructed exactly along the lines of Ref. [9], but with two important additions: (a) $F_{\rm ion}$ includes a high-T correction of the Cowan form as described in Ref. [68]. This is the SLOW decay model, with $\nu = 1/3$

in Eqs. (8) and (10). (b) The DFT average-atom model [30] for C, which we denote AA-DFT, is used for $F_{\rm elec}$. Note that while the agreement is good for $T < 20\,000$ K, as ensured by the fitting scheme of Ref. [9], the slope of E vs T for higher T is much larger in the model, indicating that the model's C_V is too large above 20 000 K. Also shown in Fig. 9 is the result of an otherwise identical model (blue lines), but with the high-T addition to $F_{\rm ion}$ chosen to be FAST [Eq. (11)]; once again, AA-DFT is used for $F_{\rm elec}$. Red points and blue lines in this plot are in far better accord. Assuming the electronic excitation contribution to be that of the AA-DFT model, this comparison is showing that a faster decay of $C_V^{\rm ion}$ is greatly favored over the slower decay previously assumed [68]. This is at least vaguely troubling, since many EOS tables in the current databases are constructed using the paradigm of QEOS [17], which assumes the Cowan model ($\nu = 1/3$, SLOW decay of $C_V^{\rm ion}$ with increasing T) for $F_{\rm ion}$. Of course, our present comparison is just for carbon, and is also for a somewhat restricted range of ρ and T. Furthermore, it is entirely possible that this conclusion depends on the electron-thermal model chosen, here AA-DFT rather than average-atom Thomas-Fermi (AA-TF) [12,17]. It is also possible that the DFT-MD data to which we compare are somehow lacking in fidelity at the higher T.

To explore both possibilities while investigating a far wider range of T, we compare to our PIMC results for E and P, as generated by the prescription outlined in Sec. II B. Figure 10 shows the fractional differences, $(X_{\rm model} - X_{\rm PIMC})/X_{\rm PIMC}$ [78], between liquid C EOS model predictions and the results of PIMC for three isochores, $\rho = 3.18$ g/cc, 8.5 g/cc, and 11.18 g/cc. Both internal energy and pressure differences are displayed. For the liquid C EOS models, we consider our four variants labeled 1–4 above: (1) SLOW/AA-DFT (green), (2) FAST/AA-DFT (red), (3) SLOW/AA-TF (magenta), (4) FAST/AA-TF (blue). Note the exceptionally wide range of T displayed in logarithmic scale on the x axis (5×10^5 K $\rightarrow 10^8$ K). Each set of points (of a given color/symbol) includes data from three isochores with densities $\rho = 3.18$ g/cc, 8.5 g/cc, and 11.18 g/cc. All model variants give results which are coincident with PIMC at sufficiently high T. However, there are significant deviations in E and P for lower temperatures. Clearly, it is the red set of points, corresponding to $F_{\rm ion} =$ FAST [Eq. (11)], $F_{\rm elec} =$ AA-DFT (average-atom DFT), which presents the smallest deviations from PIMC. Furthermore, while the preference for average-atom DFT over average-atom Thomas-Fermi *when fixing the ion-thermal model* is notable but modest, the preference for the FAST decay of $C_V^{\rm ion}$ over the SLOW ion-thermal model is quite dramatic for both choices of $F_{\rm elec}$. Finally, it is interesting that there is a pronounced peak in these fractional differences at $T \sim 10^6$ K for both E and P, and for all three isochores presented. It is possible that this arises from an ionization feature in the PIMC which is somehow manifested rather differently in the Thomas-Fermi and DFT average-atom models. However, it is also curious that these deviations attain their maxima at roughly the same T even for very different densities, since one might expect such ionization features to be rather dependent on density. The detailed shape of these curves awaits further analysis.

The conclusion of these comparisons is that both our DFT-MD and our PIMC results indicate that the rate of decay of $C_V^{\rm ion}$ to its ideal gas value is far faster than that described by

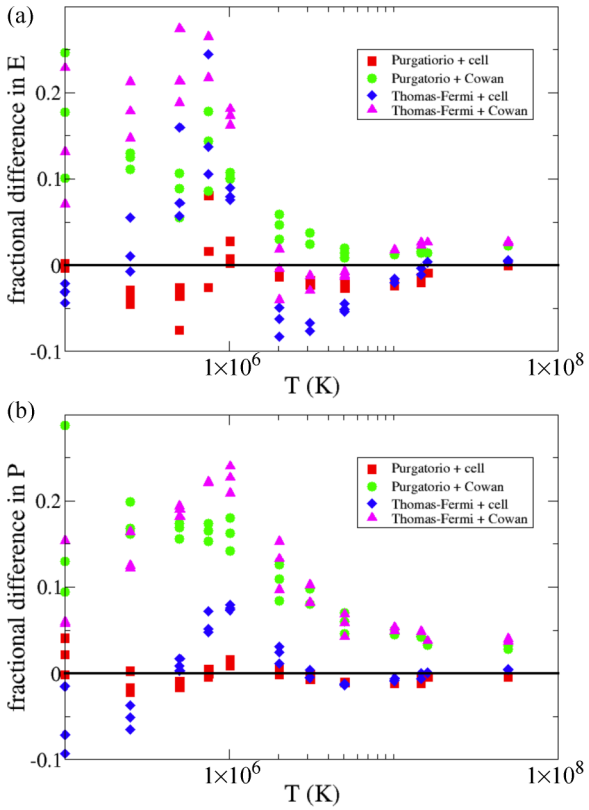

FIG. 10. (Color online) Fractional differences in internal energy (a) and pressure (b) between PIMC results for the high-T liquid/plasma and the results of our EOS model, assuming various combinations of ion-thermal and electron-thermal models. The x axis is T in K. For each liquid EOS model (indicated by color), three isochores are represented: $\rho = 3.18$, 8.5, and 11.18 g/cc. Average-atom DFT ("Purgatorio") and average-atom Thomas-Fermi ("Thomas-Fermi") comprise the choices for $F_{\rm elec}$, while SLOW ("Cowan", $\nu = 1/3$) and FAST ("cell") decays of $C_V^{\rm ion}$ with T characterize the models for $F_{\rm ion}$. See text for details.

the Cowan model [73], which assumes a $T^{-1/3}$ decay; instead we find that a far faster decay, exponential at lower T, and with a power larger than $\nu = 3/2$ at higher T, provides far better agreement for liquid C in this range of densities (3 g/cc $< \rho <$ 12 g/cc). We therefore use the FAST high-T addition to the ion-thermal free energy [Eq. (11)], together with the average-atom DFT electron-thermal model to build our liquid C free energy.

2. *Final liquid free energy model*

The parameters of our liquid cold curve (including break points [79]) and ion-thermal characteristic temperature are listed in Table II. Minimal changes have been made to the liquid free energy model of Ref. [9]. These changes include (1) an altered cold curve at high compressions, (2) the use of the DFT average-atom [30] electron-thermal term, and (3) the use of the FAST high-T addition to the Chisolm-Wallace Mie-Grüneisen [65] term [see above, Eq. (11)]. The lower pressure (<25 GPa) cold curve and the Debye-like ion-thermal model itself is unchanged from that of Ref. [9]. Figure 11 shows isotherms of internal energy for the liquid as computed

TABLE II. EOS model parameters for the liquid phase of our multiphase C EOS. The upper segment of the table concerns cold curve and ion-thermal parameters, and the lower segment contains break-point parameters used to further define the cold curve [79]. All volumes (V) are in Å^3/atom, B_0 is in GPa, B' is unitless, ϕ_0 is in eV/atom, all characteristic temperatures (θ) are in kelvins, a parameters are in eV/atom, and b and n parameters are unitless. See Ref. [69] for the specification of the break-point formula.

Parameter	Liquid
V_0	8.596
B_0	51.11
B'	5.848
ϕ_0	−7.5
V_p	6.695
θ^0	520.0
A	0.0
B	0.84
V_{b1}	3.9
n_1	3.0
a_1	−5.0
b_1	5.0
V_{b2}	2.7
n_2	3.0
a_2	10.0
b_2	3.0
V_{b3}	1.9
n_3	2.0
a_3	−40.0
b_3	5.0
V_{b4}	1.13
n_4	3.0
a_4	80.0
b_4	5.0

by both DFT-MD and our liquid EOS model. The range of V is chosen to correspond to that for which diamond and BC8 phases are stable at lower temperatures. Note that while the lowest temperature ($T = 10\,000$ K) isotherm of the model

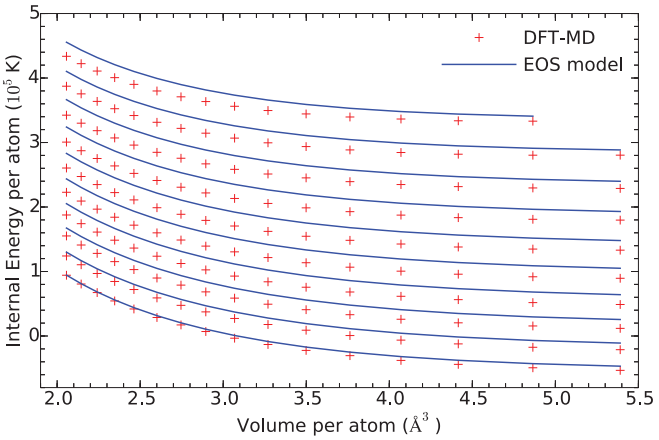

FIG. 11. (Color online) Internal energy (in K/atom) isotherms for liquid C as computed by DFT-MD (red points) and our EOS model (blue lines). Temperatures range from 10 000 K to 100 000 K.

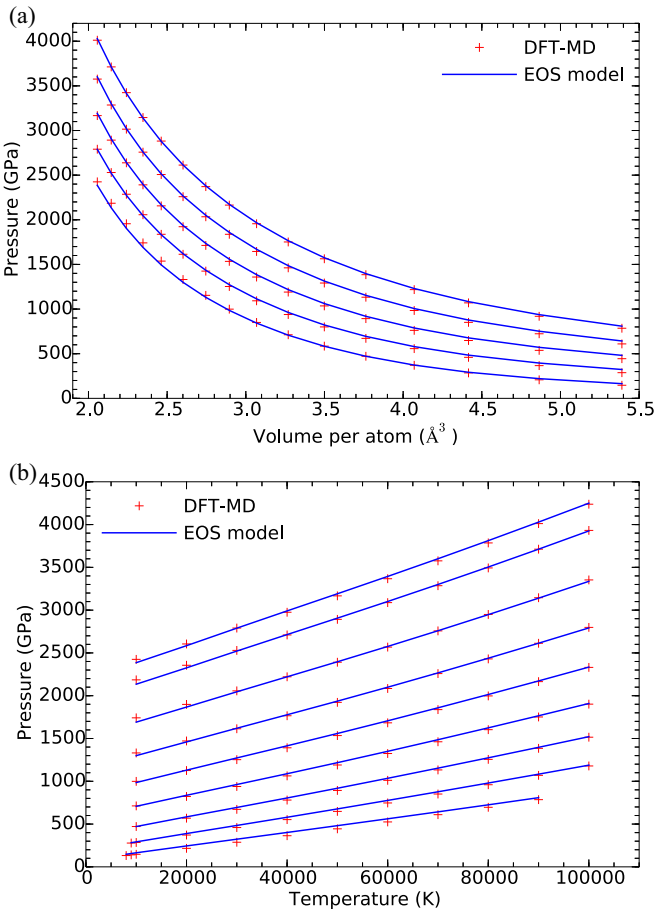

FIG. 12. (Color online) (a) Pressure (in GPa) isotherms for liquid C as computed by DFT-MD (red points) and our EOS model (blue lines). (b) Pressure (in GPa) isochores for liquid C as computed by DFT-MD (red points) and our EOS model (blue lines). The range of T represented in (a) can be seen from (b), and likewise for the range of V in (b). Note that this plot contains roughly one-half of the isotherms and isochores in this density and temperature range for which we produced DFT-MD data.

and the DFT-MD are in reasonable accord, especially for smaller V, higher-T isotherms deviate in a manner which depends on V. This results from the Chisolm-Wallace + FAST + AA-DTT models being less than perfect for C, a fact which is not surprising given their relative simplicity. Still, as we have discussed, the agreement is far better than that obtained by using the Cowan (i.e., SLOW) and/or Thomas-Fermi free energy contributions (see Figs. 9 and 10). Pressure isotherms and isochores (Fig. 12) on the same grid of (V,T) exhibit somewhat better overall agreement. The ultrahigh compression pressure isotherms of the liquid are shown in Fig. 13; agreement between our model and our DFT-MD results is also quite good, but not perfect. Our liquid EOS model uses a limited number of parameters together with simple models constructed to respect limits of extreme density and temperature. Indeed, there currently exists no general purpose approach to perfectly represent an EOS of a real material. Therefore, our model can only represent the EOS of liquid carbon up to a certain precision. For this reason,

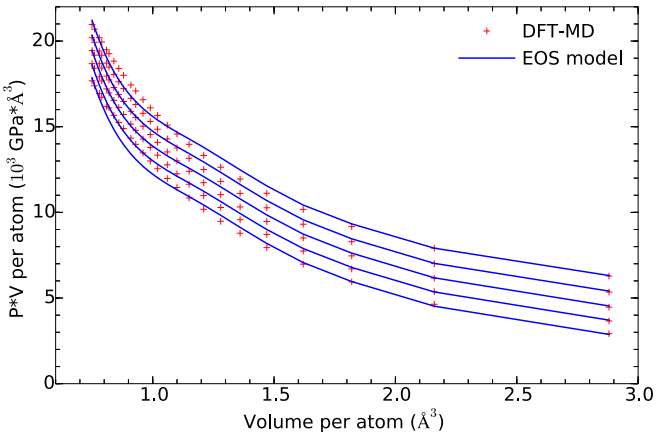

FIG. 13. (Color online) Pressure times volume per atom (in GPa×Å^3) isochores for liquid C as computed by DFT-MD (red points) and our EOS model (blue lines). The range of T represented is 10 000 K to 100 000 K. We plot $P \times V$ rather than simply P here to show more clearly the data/model discrepancies at low V. Note that this plot contains roughly one-half of the isotherms in this density range for which we produced DFT-MD data.

we report every *ab initio* EOS data point from our DFT-MD and PIMC calculations in the Supplemental Material [19]. The disagreements between our new model and these data are generally larger at higher T, where the detailed temperature- and density-dependent ionization features become important, reflecting the approximate nature of our average-atom model descriptions. Nevertheless, we note that an error in E of ∼12 000 K/atom at $T = 100\,000$ K (as seen at the highest T of Figs. 9 and 11) would give rise to an inaccuracy of a computed temperature in a continuum simulation of 12 000 K/(specific heat) ∼ 12 000 K/(2.5 kB) ∼ 5000 K. This roughly 5% error in the inferred temperature (5000 K/100 000 K) is to be compared with the much larger ∼25% error that would result from using the best available C EOS prior to this work. These subtle deviations at higher temperatures, and indeed the entire high-T range discussed at length in the previous subsection, have no bearing on the phase diagram which we now discuss, given the range of pressures over which it is considered.

C. Phase diagram

Given the free energy models for the individual solid (diamond, BC8, sc, sh) and liquid phases, we construct the phase diagram and multiphase EOS by invoking the Maxwell construction for each pair of phases (here denoted 1 and 2), and at each temperature, T, of interest [52]:

$$F_2(V_2,T) - F_1(V_1,T) = -P(V_2 - V_1), \qquad (12)$$

where $F_{1,2}$ are total free energies for each phase, $V_{1,2}$ are the transition volumes, and P is the transition pressure [80]. Figure 14(a) shows the resulting phase diagram in the regime of pressure and temperature addressed in the work of Ref. [9]. Our phase lines computed in this work differ only slightly from those in that earlier study. In particular, the diamond-BC8 transition pressure is slightly lower; this is due to our diamond and BC8 cold energies being slightly different from

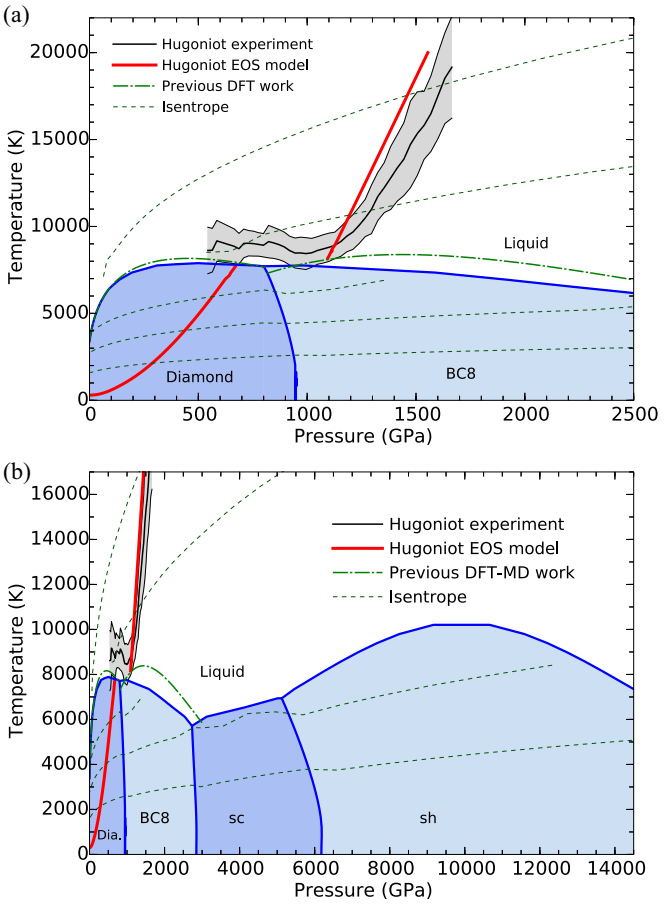

FIG. 14. (Color online) Phase diagram of C within our EOS model (phase lines are indicated by thick blue lines) for narrower (a) and wider (b) ranges of pressure. Green dashed-dotted thin lines indicate Kechin fits to the diamond and BC8 melt curves as computed in the work of Ref. [16]. The red curve shows the principal Hugoniot as predicted by our model. The shaded gray region indicates the error bars for the principal Hugoniot of Ref. [6]. Predicted isentropes are indicated by dashed green lines; entropy values, increasing from the bottom of each figure, are 3.78 k_B/atom, 5.49 k_B/atom, 6.61 k_B/atom, 12.56 k_B/atom, and 12.72 k_B/atom.

those of Ref. [9] (higher plane wave cutoffs and different pseudopotentials were used here). Also, the BC8-phase melt temperature is slightly lower, as evidenced by our comparison to the Kechin fits to the carbon melt curves of Ref. [16] to which the EOS model of Ref. [9] was fitted. Nevertheless, our phase diagram is quite close to that of the older model in the range of its applicability. Also shown in Fig. 14 are various isentropes as computed with our multiphase EOS model; values of the entropy for each are listed in the figure caption.

The principal Hugoniot of carbon computed with the model is shown as well in Fig. 14. This is defined to be the locus of final states accessible via a planar one-dimensional shock, given a particular assumed initial state, here taken to be $\rho =$ 3.52 g/cc and $T = 300$ K. This curve has two branches: one for which the final state is the diamond phase, and one in which the liquid is the final state. They are separated by a flat region in T straddling the pressure at which the diamond → BC8 transition is predicted to occur. In this portion of the

Hugoniot curve the final state is in a mixed-phase region, the size of which is directly related to the latent heat of melting, as discussed in Ref. [9]. We predict a principal Hugoniot which is similar to that predicted by the earlier carbon EOS model [9] (indeed, it is nearly identical in the diamond-phase portion). However, there is a pronounced increase (∼100 GPa) in the Hugoniot final state pressure of the liquid portion, which is explained by the added latent heat of melting resulting from the addition of electronic excitations in the metallic liquid. Our change in entropy from solid to liquid at constant V at the shock melt conditions is $\sim 3.2 k_B$/atom, while in the model of Ref. [9] it is $\sim 2.9 k_B$/atom. This in turn moves our liquid branch of the Hugoniot a bit closer to the measured T vs P Hugoniot data of Eggert *et al.* [6] [the upper and lower bounds of their experimental error bars are displayed as well in Fig. 14(a)]. While this suggests that the current EOS model may be more accurate, our predicted Hugoniot still fails to fall within the bounds of their measurements.

The phase diagram of our multiphase C EOS model over a larger range of pressure and temperature is shown in Fig. 14(b). The higher-P solid phases, sc and sh, appear as well, in addition to diamond, BC8, and liquid phases. Several important features are worth noting: (1) The BC8 → sc transition pressure is nearly independent of temperature, as is the case for the diamond → BC8 transition pressure. This is because the relevant moments, $\theta(V)$, of the PDOSs of the phases on either side of each transition are very similar at the densities at which the transitions occur, as discussed above. (2) The sc → sh phase line is less vertical, and curves to lower P for higher T, but we do not predict that this phase line intersects the BC8-sc phase line before intersecting the melt curve. This is in stark contrast to the prediction of Ref. [15], which shows a sc-sh phase line which intersects the BC8-sc line at $T \sim 5000$ K. Though we use similar *ab initio* and EOS modeling methods to theirs, we suspect that their treatment of the T dependence of the transition pressure in their Gibbs free energy matching prescription is sufficiently different from our approach to produce this discrepancy. We have checked that alternate ways of fitting our EOS data (cold energies, PDOSs, and resulting ion-thermal free energy terms) still give the general phase diagram topology we present here, though we do not discount the possibility that the extreme sensitivity of the phase lines to small changes in the individual phase free energies can render our predictions somewhat inaccurate, especially at these higher pressures where the $F(V)$ curves are nearly parallel. (3) The value of the sc-sh transition pressure at low T is ∼20% higher than that reported in Ref. [15], though the position of the BC8-sc transition line is in reasonable agreement between the two studies. This is likely a result of the use of different pseudopotentials and plane wave convergence criteria. Again, the nearly coincident free energy functions for different phases at high pressures makes the phase lines extremely sensitive to any otherwise subtle changes. (4) The melt line of the sh phase possesses a maximum at $P \sim 10\,000$ GPa. This is striking, but is one of the least certain predictions we make in this work; we have seen that slight changes to our EOS model parameters which produce small changes to our liquid free energy (which are within both our assumed model and DFT-MD uncertainties) yield sc melt temperatures which exhibit markedly different behavior.

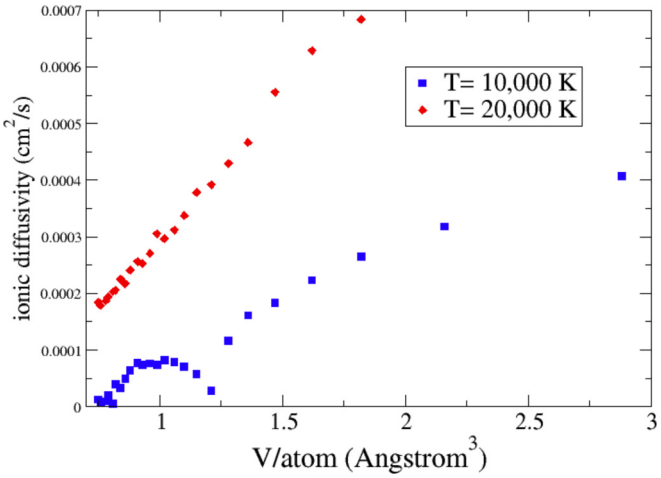

FIG. 15. (Color online) Ionic diffusivity for liquid C in cm^2/s vs V in Å^3/atom for two isotherms: $T = 10\,000$ K (lower) and $T = 20\,000$ K (upper), as computed by DFT-MD.

Our reason for favoring this particular EOS model parametrization over other nearly equivalent ones can be found in our computation of the ionic diffusivities using the DFT-MD. Figure 15 shows two diffusivity isotherms, the lower one for $T = 10\,000$ K and the upper one for $T = 20\,000$ K. A very small (approaching zero) diffusivity is indicative of a solid phase. The ionic diffusivity at 20 000 K shows the expected decrease as V decreases, but is otherwise large as expected for a liquid. The diffusivity at 10 000 K shows a pronounced dip towards zero at a $V \sim 1.2$ Å^3/atom, corresponding to a pressure of roughly 10 000 GPa (see Fig. 13). This is a clear indication of solidification, and indeed, the phase diagram of Fig. 14(b) shows a melt curve which attains its maximum (of just over 10 000 K) at $P = 10\,000$ GPa. Though this provides a nice consistency check on our DFT-MD-derived C EOS model, we caution that the diffusivity calculations were performed in a cell of 64 atoms (as were the DFT-MD calculations of EOS), and solidification can be biased in simulations with small cells of fixed shape [81].

The overarching points to be made about our prediction of the phase diagram of C are twofold: First, our predictions of phase lines are necessarily less accurate the higher the pressure is, for the reasons mentioned directly above. These inaccuracies are the combined result of the inherent uncertainties in the underlying *ab initio* electronic structure data, and the deficiencies of EOS models which have a finite number of adjustable parameters. Second, the predicted volume changes across such high-P phase lines are often exceedingly small (which is what makes the accurate determination of these transition lines difficult). Thus, the least accurate phase lines have a minimal impact on the EOS itself (P and E at a given ρ and T). We stress again that while an accurate phase diagram is desired, the primary goal of this work is the construction of an equation of state model for carbon throughout the regime of interest.

IV. COMPARISONS TO EXPERIMENTAL RESULTS

We have already discussed the comparison of the results of our C EOS model to principal Hugoniot data in the

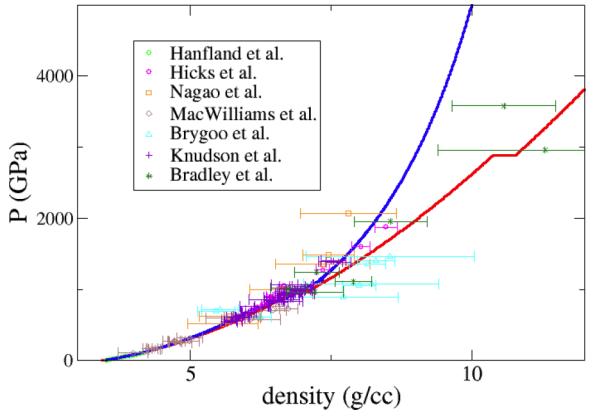

FIG. 16. (Color online) 300 K isotherm (red curve) and principal Hugoniot (blue curve) as computed by our EOS model. Green points indicate static compression data from Ref. [82], and all other symbols (plus error bars) indicate shock data from Refs. [1–5,8].

(P,T) plane. These recent measurements made use of optical pyrometry techniques [6] which lie outside the typical purview of classic shock-compression experiments. Now we compare to a larger set of principal Hugoniot data for elemental carbon transformed more typically to the (ρ,P) plane, as well as to room-temperature isotherm data from static compression experiments.

Figure 16 shows the 300 K isotherm (red) and the principal Hugoniot (blue) in (ρ,P) space as calculated from our multiphase C EOS model. The isotherm (which is very similar to the principal isentrope) shows flat regions where the phase transitions occur (BC8 $\rightarrow$ sc and sc $\rightarrow$ sh in this plot). The P vs ρ Hugoniot is nearly indistinguishable from the isotherm below roughly 1000 GPa, but deviates dramatically from it at higher stresses. The point at which they diverge corresponds to the point where the Hugoniot final states begin to reside in the liquid phase (see Fig. 14). Also shown on this figure are data from static compression measurements of the room-temperature isotherm [82] (green circles at the lowest P), magnetically driven flyer plate studies [8] (dense set of magenta + symbols with $\rho \sim 6$–7 g/cc), and multiple sets of laser-shock data on the principal Hugoniot of diamond (symbols with error bars) [1–5]. Note that much of the highest-P Hugoniot data [1] seems to straddle the 300 K isotherm, even well above $P = 1000$ GPa; indeed, the data of Brygoo *et al.* [4] even fall below our prediction of the room-T isotherm. This is very puzzling in light of our theoretical results which suggest that the Hugoniot should be much stiffer than the isotherm at these larger compressions. Our previous *ab initio*–based C EOS [9] was only fitted to DFT-MD data up to $T = 20\,000$ K, which translates to $P = 1600$ GPa on the principal Hugoniot. At this pressure, the Hugoniot and the 300 K isotherm are still rather close. The EOS model of this work, however, is validated by comparing to calculations (DFT, PIMC) that span the full range of temperature up to ideal gas conditions; note in particular the comparison to DFT-MD data on a dense grid of (ρ,T) as pictured in Figs. 11 and 12 which covers the entire range of conditions relevant for the comparison of Fig. 16.

In order to check the robustness of our conclusions that the principal Hugoniot should indeed be far stiffer than the 300 K isotherm for $P > 1000$ GPa, we have verified that the different variants of liquid C EOS we discussed in Sec. III B 1 (SLOW + AA-DFT, FAST + AA-TF, etc.) all show this same basic relationship between the low-T isotherm and the Hugoniot. Looking back again to the experimental results pictured in Fig. 16, we note that there are data with $P > 1000$ GPa that seem to be closer to our Hugoniot predictions, in particular those of Nagao *et al.* [2] and Hicks *et al.* [3]. It must be mentioned that the Hicks *et al.* data shown here is not that as presented in the original Hicks *et al.* reference, but is instead a data set which results from a reanalysis [7] of the quartz EOS [83] which was used as an impedance-matched standard in that work. The original uncorrected data set [3] lies much closer to our low-T isotherm than to our principal Hugoniot prediction in this higher-P region. These experimental improvements notwithstanding, we still submit that further work must be done to resolve the theory-experiment discrepancy at the very highest compressions shown here.

V. CONCLUSIONS

We have constructed a 5-phase EOS for elemental carbon based entirely on *ab initio* electronic structure calculations of the density functional theory and path integral Monte Carlo varieties. The PIMC and high-temperature DFT-MD data were particularly useful in quantifying the rate at which the EOS tends to the ideal gas limit as the temperature is raised. In particular, we found that these data strongly favor an EOS model in which the decay of $C_V^{\rm ion}$ is substantially faster than previously assumed [9] while also favoring a DFT average-atom description of ionization over one described by average-atom Thomas-Fermi. The multiphase EOS is constructed entirely without patching different models together in an *ad hoc* fashion; rather, full thermodynamic consistency is maintained and the appropriate high-T limit is reached in a seamless manner.

Our EOS model includes, in addition to diamond, BC8, and liquid, two of the ultrahigh pressure solid phases recently predicted by Martinez-Canales *et al.* [15]: simple cubic and simple hexagonal. Though our prediction of the phase diagram of carbon in this high-P region is broadly similar to theirs, the detailed positions of phase lines and resulting triple points are somewhat different, owing to the sensitivity of the phase lines to the detailed prescriptions for obtaining the individual phase free energies and computing the transition pressures. Further work should be done to resolve these details, though we maintain that the EOS itself should be reasonably accurate at high compressions in spite of this.

Comparison to recent laser-shock compression data [1–5] shows notable disagreement with the subset of results [1,4] which suggest that the principal Hugoniot is nearly coincident with the low-T isotherm even at pressures in excess of 1000 GPa. It is not at all clear at the moment as to what is causing such a discrepancy, particularly since the general features of our predictions (seen in Fig. 16) are quite robust and seemingly independent of many of the choices we have made in modeling the EOS of liquid C. We are encouraged, however, that a more recent reanalysis [7] of the data of Hicks

et al. [3] seems to bring their principal Hugoniot into better agreement with our prediction.

One of the central results of this work is that our high-T DFT-MD and PIMC data on carbon show that the Cowan model [17,73] of high-T liquid ion thermodynamics is likely not as accurate as previously assumed. Although the results presented here are indeed specific to carbon, existing EOS models for other materials that are based on the widely used Cowan model may need to be reexamined in this light, as those materials may also possess a somewhat rapid decay of C_V^{ion} with T. Recent work with simpler classical interionic potentials suggests that such rapid decays may be common [84].

ACKNOWLEDGMENTS

We thank C. J. Pickard, M. Martinez-Canales, P. Blaha, J. DuBois, M. A. Morales, S. B. Trickey, J. E. Pask, G. W. Collins, P. A. Sterne, H. D. Whitley, D. M. Sanchez, J. I. Castor, D. Ho, D. Braun, R. F. Smith, and B. Sadigh for helpful discussions. We also extend a special thanks to M. Millo for making available to us his reanalysis of the some of the experimental data shown in Fig. 16, to reflect the current understanding of the EOSs of the shock impedance standards. This work was performed under the auspices of the U.S. Department of Energy by Lawrence Livermore National Laboratory under Contract No. DE-AC52-07NA27344.

[1] D. K. Bradley, J. H. Eggert, D. G. Hicks, P. M. Celliers, S. J. Moon, R. C. Cauble, and G. W. Collins, Phys. Rev. Lett. **93**, 195506 (2004).

[2] H. Nagao, K. G. Nakamura, K. Kondo, N. Ozaki, K. Takamatsu, T. Ono, T. Shiota, D. Ichinose, K. A. Tanaka, K. Wakabayashi, K. Okada, M. Yoshida, M. Nakai, K. Nagai, K. Shigemori, T. Sakaiya, and K. Otani, Phys. Plasmas **13**, 052705 (2006).

[3] D. G. Hicks, T. R. Boehly, P. M. Celliers, D. K. Bradley, J. H. Eggert, R. S. McWilliams, R. Jeanloz, and G. W. Collins, Phys. Rev. B **78**, 174102 (2008).

[4] S. Brygoo, E. Henry, P. Loubeyre, J. H. Eggert, M. Koenig, B. Loupais, A. Benuzzi-Mounaix, and M. Rabec Le Gloahec, Nat. Mater. **6**, 274 (2007).

[5] R. S. McWilliams, J. H. Eggert, D. G. Hicks, D. K. Bradley, P. M. Celliers, D. K. Spaulding, T. R. Boehly, G. W. Collins, and R. Jeanloz, Phys. Rev. B **81**, 014111 (2010).

[6] J. H. Eggert, D. G. Hicks, P. M. Celliers, D. K. Bradley, R. S. McWilliams, R. Jeanloz, J. E. Miller, T. R. Boehly, and G. W. Collins, Nat. Phys. **6**, 40 (2010).

[7] R. F. Smith, J. H. Eggert, D. G. Braun, J. R. Patterson, R. E. Rudd, R. Jeanloz, T. S. Duffy, J. Biener, A. E. Lazicki, A. V. Hamza, J. Wang, T. Braun, L. X. Benedict, P. M. Celliers, and G. W. Collins [Nature (to be published)] (2014).

[8] M. D. Knudson, M. P. Desjarlais, and D. H. Dolan, Science **322**, 1822 (2008).

[9] A. A. Correa, L. X. Benedict, D. A. Young, E. Schwegler, and S. A. Bonev, Phys. Rev. B **78**, 024101 (2008).

[10] D. S. Clark, S. W. Haan, B. A. Hammel, J. D. Salmonson, D. A. Callahan, and R. P. J. Town, Phys. Plasmas **17**, 052703 (2010); S. W. Haan, J. D. Lindl, D. A. Callahan *et al.*, *ibid.* **18**, 051001 (2011).

[11] F. Lambert and V. Recoules, Phys. Rev. E **86**, 026405 (2012).

[12] S. Eliezer, A. K. Ghatak, and H. Hora, *Fundamentals of Equations of State* (World Scientific, Singapore, 2002).

[13] E. L. Pollock and D. M. Ceperley, Phys. Rev. B **30**, 2555 (1984).

[14] K. P. Driver and B. Militzer, Phys. Rev. Lett. **108**, 115502 (2012).

[15] M. Martinez-Canales, C. J. Pickard, and R. J. Needs, Phys. Rev. Lett. **108**, 045704 (2012).

[16] A. A. Correa, S. A. Bonev, and G. Galli, Proc. Natl. Acad. Sci. USA **103**, 1204 (2006). An important earlier work first suggesting the existence of a maximum in the diamond melt curve is M. P. Grumbach and R. M. Martin, Phys. Rev. B **54**, 15730 (1996).

[17] R. M. More, K. H. Warren, D. A. Young, and G. B. Zimmerman, Phys. Fluids **31**, 3059 (1988).

[18] Strictly speaking, our cold curves describe the material at $T = 0$, assuming *infinite ionic mass*; quantum zero-point motion is therefore not included in this contribution. Although the zero-point free energy (and hence, E and P as well) is independent of T, we choose to lump the zero-point energy into our ion-thermal term, since it arises from the consideration of ionic excitations.

[19] See Supplemental Material at http://link.aps.org/supplemental/10.1103/PhysRevB.89.224109 for internal energy and pressure predictions, as computed by both DFT-MD and PIMC.

[20] G. Kresse and J. Hafner, Phys. Rev. B **47**, 558 (1993); **49**, 14251 (1994); G. Kresse and J. Furthmüller, Comput. Mater. Sci. **6**, 15 (1996); Phys. Rev. B **54**, 11169 (1996).

[21] P. E. Blochl, Phys. Rev. B **50**, 17953 (1994); G. Kresse and D. Joubert, *ibid.* **59**, 1758 (1999).

[22] J. P. Perdew, K. Burke, and M. Ernzerhof, Phys. Rev. Lett. **77**, 3865 (1996); **78**, 1396(E) (1997).

[23] K. Lee, E. D. Murray, L. Kong, B. I. Lundqvist, and D. C. Langreth, Phys. Rev. B **82**, 081101(R) (2010).

[24] H. J. Monkhorst and J. D. Pack, Phys. Rev. B **13**, 5188 (1976).

[25] S. Nosé, Chem J. Phys. **81**, 511 (1984); W. G. Hoover, Phys. Rev. A **31**, 1695 (1985).

[26] N. D. Mermin, Phys. Rev. **137**, A1441 (1965).

[27] D. Vanderbilt, Phys. Rev. B **41**, 7892 (1990).

[28] P. Gianozzi *et al.*, J. Phys.: Condens. Matter **21**, 395502 (2009).

[29] P. Blaha, K. Schwarz, G. K. H. Madsen, D. Kyasnicka, and J. Luiz, *WIEN2k, An Augmented Plane Wave Plus Local Orbitals Program for Calculating Crystal Properties* (Vienna University of Technology, Vienna, 2001).

[30] B. Wilson, V. Sonnad, P. Sterne, and W. Isaacs, J. Quant. Spectrosc. Radiat. Transfer **99**, 658 (2006); D. A. Liberman, Phys. Rev. B **20**, 4981 (1979).

[31] B. Militzer and R. L. Graham, J. Phys. Chem. Solids **67**, 2136 (2006).

[32] C. Pierleoni, D. M. Ceperley, B. Bernu, and W. R. Magro, Phys. Rev. Lett. **73**, 2145 (1994).

[33] W. R. Magro, D. M. Ceperley, C. Pierleoni, and B. Bernu, Phys. Rev. Lett. **76**, 1240 (1996).

[34] B. Militzer and D. M. Ceperley, Phys. Rev. Lett. **85**, 1890 (2000).

[35] B. Militzer and D. M. Ceperley, Phys. Rev. E **63**, 066404 (2001).

[36] B. Militzer, D. M. Ceperley, J. D. Kress, J. D. Johnson, L. A. Collins, and S. Mazevet, Phys. Rev. Lett. **87**, 275502 (2001).

[37] S. X. Hu, B. Militzer, V. N. Goncharov, and S. Skupsky, Phys. Rev. Lett. **104**, 235003 (2010).

[38] S. X. Hu, B. Militzer, V. N. Goncharov, and S. Skupsky, Phys. Rev. B **84**, 224109 (2011).

[39] B. Militzer, W. Magro, and D. Ceperley, Contrib. Plasma Phys. **39**, 152 (1999).

[40] B. Militzer, Phys. Rev. B **79**, 155105 (2009).

[41] B. Militzer, Phys. Rev. Lett. **97**, 175501 (2006).

[42] B. Militzer, J. Low Temp. Phys. **139**, 739 (2005).

[43] B. Militzer and E. L. Pollock, Phys. Rev. B **71**, 134303 (2005).

[44] E. L. Pollock and B. Militzer, Phys. Rev. Lett. **92**, 021101 (2004).

[45] E. L. Pollock, Comput. Phys. Commun. **52**, 49 (1988).

[46] V. Natoli and D. M. Ceperley, J. Comput. Phys. **117**, 171 (1995).

[47] J. B. Anderson, J. Chem. Phys. **65**, 4121 (1976).

[48] P. J. Reynolds, D. M. Ceperley, B. J. Alder, and W. A. Lester, J. Chem. Phys. **77**, 5593 (1982).

[49] D. M. Ceperley, Phys. Rev. Lett. **69**, 331 (1992).

[50] The PIMC technique works efficiently even at quite low densities because no plane wave or similar expansion is needed, as employed in most DFT-MD codes.

[51] M. P. Surh, T. W. Barbee III, and L. H. Yang, Phys. Rev. Lett. **86**, 5958 (2001).

[52] D. C. Wallace, *Statistical Physics of Crystals and Liquids: A Guide to Highly Accurate Equations of State* (World Scientific, Singapore, 2003).

[53] A. A. Correa, L. X. Benedict, M. A. Morales, J. I. Castor, P. A. Sterne, and E. Schwegler (unpublished).

[54] L. X. Benedict, T. Ogitsu, A. Trave, C. J. Wu, P. A. Sterne, and E. Schwegler, Phys. Rev. B **79**, 064106 (2009).

[55] P. Vinet, J. H. Rose, J. Ferrante, and J. R. Smith, J. Phys.: Condens. Matter **1**, 1941 (1989).

[56] M. A. Morales, J. M. McMahon, C. Pierleoni, and D. M. Ceperley, Phys. Rev. B **87**, 184107 (2013); Phys. Rev. Lett. **110**, 065702 (2013).

[57] B. Santra, J. Klimes, D. Alfe, A. Tkatchenko, B. Slater, A. Michaelides, R. Car, and M. Scheffler, Phys. Rev. Lett. **107**, 185701 (2011).

[58] J. P. Perdew and Wang Yue, Phys. Rev. B **33**, 8800(R) (1986).

[59] A. Zupan, K. Burke, M. Ernzerhof, and J. P. Perdew, J. Chem. Phys. **106**, 10184 (1997).

[60] C. W. Greeff, M. J. Graf, J. C. Boettger, and J. D. Johnson, AIP Conf. Proc. **845**, 89 (2006).

[61] This representation of the double-Debye free energy, written in terms of θ_A, θ_B, and θ_1, differs from the form shown in Ref. [9], which is written in terms of θ_A, θ_B, and θ_0. But they are entirely equivalent.

[62] It is important to note that GGA-DFT generally underestimates the electronic excitation gaps of materials, resulting in metalization pressures that are too low, and electronic excitation free energies (for systems on the border between insulating and metallic) which are too large. In this sense, our predictions of the effects of electronic excitation on the EOS of solid C are likely to be overestimates.

[63] For all solid phases whose models possess a T^2 (electron-thermal or anharmonic ion-thermal) free energy term, we apply corrections above $T = 20\,000$ K, well beyond their ranges of stability, which smoothly force $F_{\rm ion}$ to a constant independent of T. This is done to prevent these solid phases from becoming more stable than the liquid at high T, which would eventually occur if the T^2 term, meant strictly as a low-T correction, is allowed to persist at high temperatures.

[64] This is in contrast to the example discussed in this work on iron at high pressures: L. Stixrude, Phys. Rev. Lett. **108**, 055505 (2012).

[65] E. D. Chisolm and D. C. Wallace, J. Phys.: Condens. Matter **13**, R739 (2001).

[66] E. D. Chisolm, S. D. Crockett, and D. C. Wallace, Phys. Rev. B **68**, 104103 (2003).

[67] S. Hamel *et al.*, Phys. Rev. B **86**, 094113 (2012).

[68] L. X. Benedict, Lawrence Livermore National Laboratory Technical Report LLNL-TR-425047, 2010.

[69] For a given break point, the cold curve function is changed according to $E_{\rm cold}(V) \rightarrow E_{\rm cold}(V) + \frac{a[(V_b/V)-1]^n}{b+[(V_b/V)-1]^n}$ for $V < V_b$, and no correction for $V > V_b$. When there are multiple break points applied for a given phase (there are four in our liquid model), it is understood that these additions are applied in succession (i.e., first "1", then "2", etc.).

[70] D. Lai, A. M. Abrahams, and S. L. Shapiro, Astrophys. J. **377**, 612 (1991).

[71] D. A. Liberman, Phys. Rev. B **20**, 4981 (1979).

[72] See C. E. Starrett and D. Saumon, Phys. Rev. E **87**, 013104 (2013), and references therein.

[73] C. W. Cranfill and R. More, Los Alamos Scientific Laboratory Report LA 7313-MS, 1978.

[74] Note that $T_M(V)$ is not the melting temperature of C (as in the original Cowan prescription used in Ref. [17]), but is rather the temperature above which the ion-thermal specific heat begins to deviate from the Dulong-Petit limit of $3k_B$ and head toward the ideal gas value of $3/2k_B$ [68]. Note also that the conclusions we draw in this work regarding the lack of suitability of the Cowan model also apply if we lower the value of $T_M(V_0)$ to 10 000 K, which is just above the melt temperature of C over a wide range of compressions.

[75] F. A. Lindemann, Phys. Z **11**, 609 (1910).

[76] J. D. Johnson and D. A. Young (private communication).

[77] A. A. Correa, L. X. Benedict, S. Hamel, and E. Schwegler (unpublished).

[78] Our definitions for the fractional differences in E and P would be problematic if $E_{\rm PIMC}$ or $P_{\rm PIMC}$ were close to zero for some T; this is not the case for the T and ρ considered here (and given the definition of the zero of internal energy employed).

[79] We note that the break point with the smallest volume ($V_{b4} = 1.13$ Å^3/atom) is added to appease agreement with our highest compression DFT-MD data; however, it is important to point out that this final break point should only be added if the EOS model is used up to a maximum pressure of 14 000 GPa. If the EOS model is to be used for pressures greater than this, that final break point should be eliminated in order to prevent unphysical behavior due to its effects at still higher compressions.

[80] Since the individual solid phases are only meaningful (as in metastable) in the neighborhood of their fields of thermodynamic stability, we only consider each solid phase free energy function throughout a restricted range of V, so as to minimize the spurious effects of improper extrapolation. In particular, we consider diamond from 2.5 Å^3/atom $\rightarrow$ 7.0 Å^3/atom, BC8 from 1.3 Å^3/atom $\rightarrow$ 3.5 Å^3/atom, sc from 1.0 Å^3/atom $\rightarrow$ 7.0 Å^3/atom, and sh from 0.01 Å^3/atom (undoubtedly well

beyond its actual range of stability) $\rightarrow$ 7.0 Å^3/atom. The liquid is considered throughout the wide range 0.01 Å^3/atom $\rightarrow$ 7.0 Å^3/atom, though the actual intended range of validity of the EOS model reported here is limited to the regime covered by our *ab initio* calculations (see Supplemental Material [19]): 0.75 Å^3/atom $< V <$ 5.4 Å^3/atom (as we stated above, we choose not to require agreement with the 0.1 g/cc PIMC isochore in this work).

[81] We have also computed the internal energy of an isochore with $V = 1.21$ Å^3/atom using DFT-MD, and have shown that there is a pronounced jump in E as T is raised above 10 000 K, which again is right in the neighborhood of the maximum of the melt curve of the sh phase. For this set of calculations, a periodic cell with 392 C atoms was used.

[82] M. Hanfland, H. Beister, and K. Syassen, Phys. Rev. B **39**, 12598 (1989). Note that this work described static compression of graphite; however for densities above ~3.5 g/cc, a clear transition to diamond-like compressibility is seen.

[83] D. G. Hicks, T. R. Boehly, P. M. Celliers, J. H. Eggert, E. Vianello, D. D. Meyerhofer, and G. W. Collins, Phys. Plasmas **12**, 082702 (2005); M. D. Knudson and M. P. Desjarlais, Phys. Rev. Lett. **103**, 225501 (2009).

[84] D. Bolmatov, V. V. Brazhkin, and K. Trachenko, Nat. Commun. **4**, 2331 (2013).